

---

# CRAFT: Clinical Reward-Aligned Finetuning for Medical Image Synthesis

---

Yunsung Chung<sup>1</sup> Alex El Darzi<sup>2</sup> Carlo El Houry<sup>2</sup>  
Han Feng<sup>2</sup> Nassir Marrouche<sup>2</sup> Jihun Hamm<sup>1</sup>

<sup>1</sup>Department of Computer Science, Tulane University, New Orleans, LA 70118

<sup>2</sup>School of Medicine, Tulane University, New Orleans, LA 70112

{ychung3, jhamm3}@tulane.edu

## Abstract

Foundation diffusion models can generate photorealistic natural images, but adapting them to medical imaging remains challenging. In medical adaptation, limited labeled data can exacerbate hallucination-like and clinically implausible synthesis, while existing metrics such as FID or Inception Score do not quantify per-image alignment with pathology-relevant criteria. We introduce the Clinical Alignment Score (CAS), a foundation-model-based proxy for clinical alignment that evaluates generated images along four complementary dimensions beyond visual fidelity. Building on CAS, we propose Clinical Reward-Aligned Finetuning (CRAFT), a reward-based adaptation framework that transfers medical knowledge from multimodal large language models and vision-language models through label-conditioned prompt enrichment, clinical checklists, and differentiable reward optimization. Across four diverse modalities, CRAFT improves CAS and downstream classification performance over strong adaptation baselines. Beyond average CAS gains, CRAFT reduces the empirical low-alignment tail below a real-image reference threshold by 5.5–34.7% points relative to the strongest baseline, corresponding to a 20.4% average relative reduction across datasets. These results indicate fewer hallucination-like generations under CAS, and are corroborated by out-of-family evaluator evaluation, structured checklist auditing, memorization analysis, and a blinded physician preference study on CheXpert.

## 1 Introduction

Deep learning has demonstrated remarkable success in medical decision-making, including dermatology and radiology [Anderson et al., 2024, Esteva et al., 2017, Brinker et al., 2019, Liu et al., 2020, Soenksen et al., 2021]. However, robust medical model training remains constrained by limited labeled data, privacy barriers, annotation cost, and long-tailed clinical distributions.

Synthetic data generation has emerged as a partial remedy to medical data scarcity [Chung et al., 2025]. Diffusion models [Ho et al., 2020] have been adapted from general [Gal et al., 2022, Kim et al., 2022, Li et al., 2023, Ruiz et al., 2023, Ye et al., 2023, Zhang et al., 2023] to medical domains, including chest X-ray, brain MRI, CT, and dermatology [Ali et al., 2022,

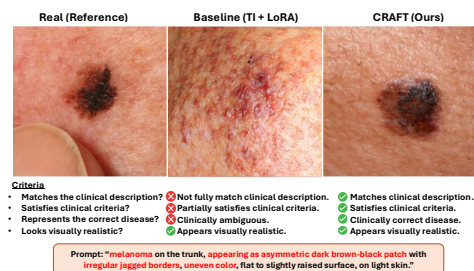


Figure 1: Melanoma example. The baseline synthesis lacks clear pathology-specific cues, while CRAFT exhibits stronger alignment with the clinical criteria captured by CAS.

Huang et al., 2024, Khader et al., 2023, Pinaya et al., 2022, Guo et al., 2025, Xu et al., 2024, Wang et al., 2025]. Synthetic data can also improve downstream utility or mitigate distribution shifts in some settings [Chung et al., 2024, Wang et al., 2024, Ktena et al., 2024].

In medical imaging, visual realism is insufficient: a generated image can look plausible while missing the pathology-specific findings that make it clinically useful. Distribution-level metrics such as Fréchet Inception Distance (FID) [Heusel et al., 2017], Inception Score (IS) [Salimans et al., 2016], and Kernel Inception Distance [Bińkowski et al., 2018] measure set-level visual fidelity, while LPIPS [Zhang et al., 2018] and CLIPScore [Hessel et al., 2021] measure perceptual or text-image alignment. None directly evaluates whether a generated image satisfies pathology-relevant criteria for a given clinical prompt (see Figure 1).

To close this gap, we propose the Clinical Alignment Score (CAS), a foundation-model-based proxy for clinical alignment. CAS combines four primitives: Visual Description Consistency (VDC), Clinical Criteria Satisfaction (CCS), Diagnostic Discriminability (DD), and Semantic Feature Similarity (SFS). Unlike generic perceptual metrics, CAS targets clinically meaningful failure modes via text–image alignment, checklist satisfaction, diagnostic separability, and reference-anchored semantic similarity, and it requires no manual preference labels. CAS remains a proxy, not a substitute for expert review.

Building on CAS, we introduce CRAFT (Clinical Reward-Aligned Finetuning), which turns the same clinical dimensions into differentiable training signals. CRAFT adapts a general-purpose diffusion model toward clinically aligned medical synthesis under limited supervision. Specifically, we use MLLMs (e.g., MedGemma [Sellingren et al., 2025], GPT-4o [Achiam et al., 2023]) to expand sparse clinical labels into image-grounded descriptions and create disease-level clinical criteria, and also use VLMs (e.g., MedSigLIP [Sellingren et al., 2025]) as a differentiable critic that supplies reward feedback during finetuning. Across four medical imaging datasets, CRAFT achieves higher CAS on held-out test cases than the compared adaptation baselines, and also improves real+synthetic downstream classification performance. On CheXpert, CRAFT samples are rated higher by medical experts, supporting improved clinical plausibility beyond simple memorization. While we focus on medical imaging, the framework should extend naturally to other domains with expert-defined semantic criteria—e.g., satellite imagery, materials science, or industrial inspection.

Clinical alignment must be evaluated not only by average performance but also by failure tails. In medical image synthesis, even a small fraction of hallucination-like samples can inject misleading pathology cues into downstream training. We therefore define a low-alignment rate using a real-image reference threshold and analyze the lower tail of per-image CAS. Across four datasets, CRAFT reduces this low-alignment rate by 5.5–34.7% points relative to the strongest baseline, indicating that clinical reward alignment improves not only average quality but also tail reliability.

Our contributions are threefold. (1) We introduce CAS, a decomposed foundation-model-based proxy for clinical alignment that combines VDC, CCS, DD, and SFS. (2) We propose CRAFT, a reward-aligned finetuning framework that transfers structured medical knowledge from MLLMs and VLMs into a diffusion model through prompt enrichment and differentiable reward optimization. (3) Across dermatology, radiology, histopathology, and retinal fundus imaging, CRAFT improves average CAS, reduces low-CAS failure rates, and improves downstream classification accuracy. We corroborate these gains with out-of-family evaluator analysis, checklist auditing, diversity analysis, and blinded physician preference study on CheXpert.

## 2 Related works

**Medical image synthesis.** Latent diffusion models [Rombach et al., 2022] have been adapted to medical imaging domains such as chest X-rays [Ali et al., 2022, De Wilde et al., 2023, Huang et al., 2024], 3D brain MRI [Khader et al., 2023, Pinaya et al., 2022], and CT [Guo et al., 2025, Zhao et al., 2025]. Beyond high-fidelity, synthetic data can improve robustness in data-scarce regimes [Wang et al., 2025], and mitigate demographic distribution shifts [Ktena et al., 2024, Wang et al., 2024]. To introduce semantic control, prior work adapts pretrained diffusion models using Textual Inversion [Gal et al., 2022] and/or LoRA [Hu et al., 2022] to inject disease concepts into pre-trained models [De Wilde et al., 2023, Wang et al., 2024, Fayyad et al., 2025]. However, optimizing for distributional realism or reconstruction fidelity alone does not guarantee pathology-specific correctness. Prior work

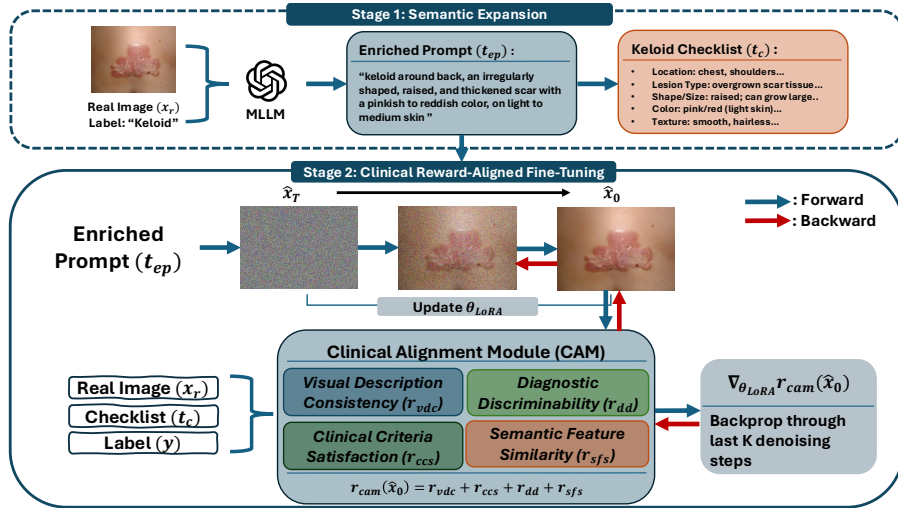


Figure 2: Overview of the CRAFT Framework. The pipeline consists of two stages: (1) Semantic Enrichment uses an MLLM to generate an image-grounded enriched prompt ( $t_{ep}$ ) from each image-label pair ( $x_i, y_i$ ) and a class-level checklist ( $t_c$ ) from the label  $y_i$ . (2) Clinical Reward-Aligned Finetuning optimizes a pretrained diffusion model using a VLM critic, which computes differentiable rewards for visual description consistency ( $r_{vdc}$ ), clinical criteria satisfaction ( $r_{ccs}$ ), diagnostic discriminability ( $r_{dd}$ ), and semantic feature similarity ( $r_{sfs}$ ). Reward gradients are backpropagated through the final  $K$  denoising steps, updating only LoRA parameters for efficient training.

has shown that medical image translation and synthesis systems can introduce hallucinated features when objectives fail to preserve clinically meaningful structure [Cohen et al., 2018].

**Reward and preference alignment.** Diffusion model alignment increasingly uses reward or preference signals, extending ideas such as DPO [Rafailov et al., 2023] to images via offline preference learning and reward modeling [Wallace et al., 2024, Xu et al., 2023]. Existing methods include classifier/reward-model-based alignment [Bai et al., 2025, Li et al., 2024, 2025, Wallace et al., 2024] and direct optimization through the denoising process [Black et al., 2023, Clark et al., 2023]. In medical imaging, Sun et al. [2023] leverages direct pathologist feedback, while subsequent work explores automated feedback: Wang et al. [2025] utilizes DPO to align skin lesion synthesis, and Saremi et al. [2025] optimizes against online classifiers but relies on discrete reward proxies. CRAFT differs in jointly combining label-conditioned prompt enrichment, class-level clinical checklists, reference-anchored semantic rewards, and differentiable reward optimization within a unified framework, and in evaluating across four imaging domains rather than one.

### 3 Methods

Diffusion models pretrained on general-domain images provide strong priors over natural image statistics but lack the domain-specific knowledge needed to interpret sparse clinical labels. To bridge this gap, we propose CRAFT (Clinical Reward-Aligned Finetuning), which adapts a general-purpose diffusion model toward clinically aligned medical image synthesis through two stages (Figure 2).

#### 3.1 Stage 1: LLM-Driven semantic enrichment

Let  $D = \{(x_i, y_i)\}$  be a dataset of medical images with sparse clinical labels  $y_i \in Y$ . Conditioned on  $y_i$  alone, a pretrained diffusion model often produces generic or clinically inconsistent samples, reflecting the limited coverage of medical concepts in its pretraining data. We address this with MLLM-generated descriptions that ground each sparse label in the paired training image. For each image-label pair  $(x_i, y_i)$ , we generate two complementary textual artifacts:

**Enriched Prompt ( $t_{ep}$ ).** A per-image visual description generated by the MLLM that captures instance-specific visual attributes of  $x_i$ , such as morphology, color variation, and border characteristics, in a domain-dependent manner. The ground-truth label  $y_i$  is provided as a constraint during prompt generation to suppress diagnostic hallucination and enforce consistency with the underlying pathology. This enriched prompt translates an abstract label into image-grounded visual cues understandable by non-expert models (e.g., “an asymmetric hyperpigmented lesion with irregular jagged borders”), enabling the diffusion model to condition on fine-grained, instance-level appearance (Appendix B).

**Natural Language Checklist ( $t_c$ ).** A per-disease structured checklist that encodes label-level clinical criteria shared across all images of class  $y$  (e.g., required shape, texture, and color). Unlike  $t_{ep}$ , which varies across images,  $t_c$  is fixed for each disease and serves as a stable clinical constraint that enforces clinical consistency across generations (Appendix C).

### 3.2 Stage 2: clinical reward-aligned finetuning

In the second stage, we finetune the diffusion model parameters  $\theta$  by combining the standard diffusion objective with a clinical reward computed by a frozen VLM critic. Because Stable Diffusion is a latent diffusion model, the diffusion reconstruction term is computed in VAE latent space [Kingma and Welling, 2013], while clinical rewards are computed after decoding the generated latent into pixel space.

Let  $z_r = \mathcal{E}_{\text{VAE}}(x_r)$  denote the VAE latent of a real training image  $x_r$ , and let  $z_t = \alpha_t z_r + \sigma_t \epsilon$  be the noised latent at diffusion timestep  $t$ . The text condition is the enriched prompt  $c = t_{ep}$ . During reward optimization, differentiable sampling through the final  $K$  denoising steps produces a generated latent  $\hat{z}_0$ , which is decoded into an image  $\hat{x}_0 = \mathcal{D}_{\text{VAE}}(\hat{z}_0)$  before computing VLM-based rewards. The training objective is:

$$\mathcal{L}(\theta) = \mathbb{E}_{z_r, c, t, \epsilon} [\lambda_{\text{diff}} \|\epsilon - \epsilon_\theta(z_t, t, c)\|_2^2 - \lambda_{\text{cam}} r_{\text{cam}}(\hat{x}_0, x_r, c, t_c, y)]. \quad (1)$$

The reference image  $x_r$  is used for the diffusion reconstruction term and SFS reward during training, but not provided to the generator at test-time synthesis. To preserve the model’s generative priors, we employ LoRA to optimize only low-rank decomposition matrices added to the attention layers. Gradients from  $r_{\text{cam}}$  are propagated through the sampled image  $\hat{x}_0$  and the final  $K$  denoising steps while the VLM encoders remain fully frozen, similar to DRaFT- $K$  [Clark et al., 2023].

The reward  $r_{\text{cam}}$  is computed by the Clinical Alignment Module (CAM) as a sum of four components: **Objective 1: Visual Description Consistency (VDC) Rewards.** To ensure that the synthesized image reflects the fine-grained visual attributes described in the enriched prompt generated in Stage 1, we maximize the cosine similarity between the image embedding  $E_I(\hat{x}_0)$  and the text embedding of the image-grounded enriched prompt  $t_{ep}$ :

$$r_{\text{vdc}} = \cos(E_I(\hat{x}_0), E_T(t_{ep})) \quad (2)$$

This reward enforces alignment with *instance-specific* morphology, color variation, and structural details, preserving fine-grained semantic fidelity while leaving room for visual diversity across samples.

**Objective 2: Clinical Criteria Satisfaction (CCS) Rewards.** To ensure adherence to disease-specific clinical criteria shared across samples of the same label, we additionally enforce alignment with structured clinical criteria expressed as a natural language checklist  $t_c$ :

$$r_{\text{ccs}} = \cos(E_I(\hat{x}_0), E_T(t_c)) \quad (3)$$

Unlike  $r_{\text{vdc}}$ , which captures instance-level appearance,  $r_{\text{ccs}}$  enforces *class-level* clinical consistency, such as required lesion morphology or anatomical patterns. This separation enables the model to generate visually diverse samples while encouraging alignment with disease-specific visual criteria.

**Objective 3: Diagnostic Discriminability (DD) Reward.** Visual similarity to text does not guarantee diagnostic separability. To ensure the generated features are discriminative for the correct pathology  $y$ , we employ a linear probe  $\phi$  trained on the frozen VLM embedding space using the same training split used to finetune the diffusion model. We define the reward as the log-likelihood of the correct

class:

$$r_{\text{dd}} = \log \frac{\exp(\phi(E_I(\hat{x}_0))_y)}{\sum_{k=1}^C \exp(\phi(E_I(\hat{x}_0))_k)} \quad (4)$$

Maximizing this reward penalizes generations that look realistic but lack the feature combinations required for confident diagnosis.

**Objective 4: Semantic Feature Similarity (SFS) Reward.** A common failure mode in synthetic medical data is hallucinatory drift: models produce exaggerated depictions that lack the fine-grained textural fidelity of real pathology [Cohen et al., 2018]. To discourage such drift, we introduce a reference-anchored semantic similarity objective that operates in a frozen medical VLM embedding space. For each training step, the generated sample  $\hat{x}_0$  is paired with its corresponding real reference image  $x_r$ :

$$r_{\text{sfs}} = \cos(E_I(\hat{x}_0), E_I(x_r)) \quad (5)$$

$r_{\text{sfs}}$  anchors generations to real medical-image representation and discourages semantic drift toward exaggerated or unrealistic pathology. It is used during paired training and reference-based evaluation, but not for prompt-only deployment. Appendix M finds no pixel-level or feature-space memorization.

### 3.3 Optimization via DRaFT

We optimize  $r_{\text{cam}}$  using DRaFT- $K$  [Clark et al., 2023], which backpropagates reward gradients only through the final  $K$  denoising steps, reducing memory cost and instability. We update only LoRA parameters and keep the VLM encoders frozen. To reduce gradient variance from stochastic sampling, we generate  $M$  trajectories per prompt and average rewards:

$$r_{\text{cam}} = \frac{1}{M} \sum_{m=1}^M \frac{1}{4} \left( r_{\text{vdc}}^{(m)} + r_{\text{ccs}}^{(m)} + r_{\text{dd}}^{(m)} + r_{\text{sfs}}^{(m)} \right). \quad (6)$$

We use  $\lambda_{\text{diff}} = 0.2$  and  $\lambda_{\text{cam}} = 0.8$ , giving each reward component an effective weight of 0.2 in the full objective. Appendix J reports DD-weight sensitivity.

## 4 Experiments

### 4.1 Experimental setup

#### 4.1.1 Datasets

We evaluate CRAFT on four medical imaging domains with distinct visual characteristics.

**Fitzpatrick17k.** We use the 20-condition subset of Fitzpatrick17k [Groh et al., 2021] following [Wang et al., 2025], with a 50/50 patient-level split (3,100 train / 3,100 test).

**CheXpert.** Following [Chung et al., 2025], we use a 4-class frontal-view CheXpert subset [Irvin et al., 2019] (*Cardiomegaly, Pleural Effusion, Pneumonia, No Finding*), totaling 990 images (495 train / 495 test).

**BreakHis.** We use the  $100\times$  BreakHis subset [Xie et al., 2019] with 8 diagnostic categories and a 50/50 split (1,040 train / 1,041 test).

**ORIGA.** We use the ORIGA retinal fundus dataset [Zhang et al., 2010] with glaucoma / non-glaucoma labels, following the official split (454 train / 196 evaluation).

#### 4.1.2 Baselines

We compare against SD2.1 zero-shot, Textual Inversion (TI) [De Wilde et al., 2023], TI+LoRA [Wang et al., 2024], and DPO-style preference optimization [Wang et al., 2025]. Following Wang et al. [2025], DPO uses 1,024 offline preference pairs per dataset, with MedGemma selecting the preferred image from two seed-varied LoRA samples per pair. We include zero-shot Janus-Pro and Flux as general-purpose references in Appendix L.

Table 1: Quantitative results across four medical imaging domains. Synthetic-method values are means over five seeds. The “Real” row is a reference point, not a target (see Sec. 4.2.1). CRAFT achieves the best CAS on all four datasets.

Method	Fitzpatrick17k					CheXpert					BreakHis					ORIGA				
	VDC	CCS	DD	SFS	CAS	VDC	CCS	DD	SFS	CAS	VDC	CCS	DD	SFS	CAS	VDC	CCS	DD	SFS	CAS
Real	.168	.135	.666	1.00	.492	.149	.148	.511	1.00	.452	.154	.135	.753	1.00	.511	.132	.171	.781	1.00	.521
Zero-Shot	.072	.059	.125	.550	.202	.051	.036	.258	.477	.205	.053	.079	.368	.676	.294	.063	.083	.648	.658	.363
DPO	.093	.121	.350	.760	.331	.060	.119	.252	.848	.320	.121	.124	.413	.852	.378	.080	.156	.734	.878	.462
TI	.092	.119	.339	.757	.327	.060	.119	.255	.848	.320	.128	.104	.418	.820	.367	.127	.153	.697	.847	.456
TI+LoRA	.094	.150	.449	.809	.376	.057	.142	.276	<b>.941</b>	.354	.142	.120	.477	.872	.402	.137	.170	.800	.880	.497
<b>CRAFT</b>	<b>.166</b>	<b>.158</b>	<b>.520</b>	<b>.824</b>	<b>.417</b>	<b>.145</b>	<b>.146</b>	<b>.375</b>	.939	<b>.401</b>	<b>.153</b>	<b>.136</b>	<b>.486</b>	<b>.894</b>	<b>.417</b>	<b>.147</b>	<b>.177</b>	<b>.842</b>	<b>.895</b>	<b>.515</b>

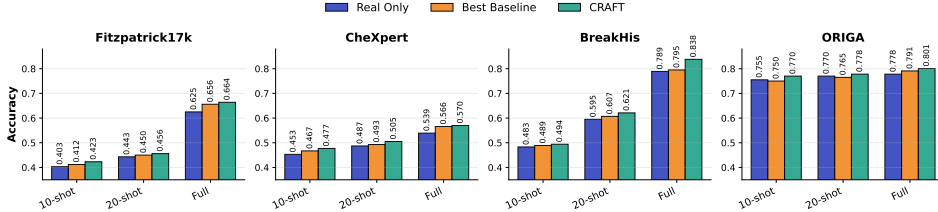


Figure 3: Downstream classification accuracy in a real+synthetic augmentation setting (20% synthetic per batch) across four datasets and three data scales. CRAFT achieves the best accuracy in every setting. “Best Baseline” refers to the strongest non-reward method (TI+LoRA) per setting.

### 4.1.3 Implementation details

All generators use Stable Diffusion v2.1 at  $512 \times 512$  resolution. We first learn disease-specific textual inversion tokens for 3,000 steps, then apply LoRA to UNet cross-attention layers and train for 10 epochs. CRAFT uses DRaFT- $K$  with  $K = 1$ ,  $M = 2$  stochastic repeats, and batch size 4. Additional training details are provided in Appendix A.

**Prompting and checklists.** Enriched prompts ( $t_{ep}$ ) and class-level checklists ( $t_c$ ) are generated offline from paired image-label data and then held fixed during optimization. Prompting details (B) and templates (C) are in the Appendix.

**Evaluation protocol.** Our main CAS evaluation follows a prompt-conditioned re-synthesis protocol: each held-out image is first converted into a label-constrained textual description, and the same text prompt is provided to every generator. The image pixels are never used as generator input and are used only after synthesis for reference-based metric computation such as SFS.

### 4.1.4 Evaluation metrics

To reduce evaluator leakage, CRAFT uses MedSigLIP as the frozen training critic, while all main quantitative metrics are computed with a separate SigLIP encoder not used for optimization. We further test robustness with MetaCLIP2 in Sec. 4.2.7; model-role separation is summarized in Table 11.

**VDC/CCS/SFS.** VDC and CCS are image–text cosine similarities between the generated image and the enriched prompt  $t_{ep}$  or class-level checklist  $t_c$ , respectively. SFS is image–image cosine similarity between the generated image and its paired real reference in the evaluator embedding space.

**DD.** For training, the DD reward uses a linear probe trained on frozen MedSigLIP embeddings from real training images. For evaluation, we train a separate probe on frozen SigLIP embeddings and report classification accuracy on generated samples.

**CAS.** CAS is the macro-average of the four primitive scores (VDC, CCS, DD, SFS) on the held-out test split, with each primitive computed in the SigLIP evaluator’s embedding space. Since CAS is a foundation-model-based proxy rather than clinical ground truth, we report primitive components and complement CAS with MetaCLIP2 evaluation, diversity analysis, downstream augmentation, checklist auditing, low-alignment tail analysis, and physician preference evaluation.

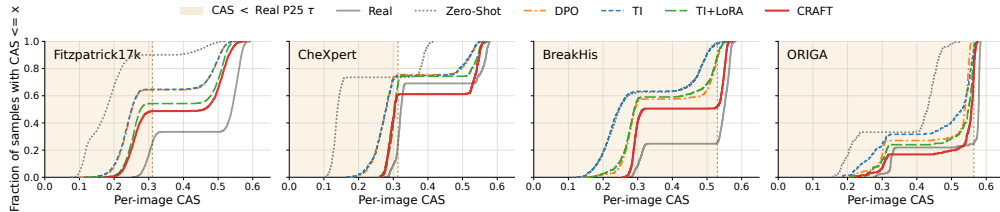


Figure 4: Empirical CDFs of per-image CAS. The shaded region denotes CAS below  $\tau$ , where  $\tau$  is the 25th percentile of the real-image CAS distribution for each dataset. Lower curves in the shaded region indicate fewer low-alignment generations. CRAFT consistently reduces the lower-tail region across all four datasets.

## 4.2 Main results

We evaluate CRAFT on four distinct medical domains: dermatology (Fitzpatrick17k), radiology (CheXpert), histopathology (BreakHis), and retinal fundus imaging (ORIGA). We report CAS as the primary proxy for clinical alignment, and use downstream augmentation, out-of-family evaluation, checklist auditing, preference evaluation, and ablations as complementary evidence.

### 4.2.1 Quantitative analysis

Table 1 shows that CRAFT achieves the highest CAS among compared adaptation methods across all four domains. Relative to TI+LoRA, CRAFT improves CAS from 0.376 to 0.417 on Fitzpatrick17k, 0.354 to 0.401 on CheXpert, 0.402 to 0.417 on BreakHis, and 0.497 to 0.515 on ORIGA. The largest gains occur on Fitzpatrick17k and CheXpert, where clinically relevant morphology and subtle radiographic findings are difficult to convey from sparse labels alone. On Fitzpatrick17k, CRAFT improves diagnostic discriminability over TI+LoRA (0.520 vs. 0.449), while on CheXpert, it substantially improves VDC (0.145 vs. 0.057), indicating stronger evaluator-measured alignment between generated images and clinical text conditions.

The “Real” row is not a theoretical upper bound on every component: VDC and CCS depend on text–image embedding alignment and checklist phrasing, while SFS is 1.0 by construction (each real image is compared to itself).

### 4.2.2 Low-alignment tail analysis

Average CAS can hide clinically important failure cases, so we examine the lower tail directly. For each dataset, we set  $\tau$  to the 25th percentile of the real-image CAS distribution; generated samples below  $\tau$  fall below the lower quartile of real-image alignment under CAS. Figure 4 shows that CRAFT shifts the per-image CAS distribution toward higher values and reduces the low-alignment region across all four datasets. CRAFT reduces the low-CAS rate relative to the strongest baseline from 54.2% to 48.7% on Fitzpatrick17k, 68.9% to 60.8% on CheXpert, 86.8% to 52.1% on BreakHis, and 89.8% to 77.0% on ORIGA, corresponding to an average relative reduction of 20.4%. CRAFT therefore improves not only mean alignment but also tail reliability. Full per-method tail statistics are provided in Appendix H.

### 4.2.3 Effect of prompt enrichment

To isolate prompt enrichment from reward optimization, Table 2 compares TI+LoRA, TI+LoRA+ $t_{ep}$ , and CRAFT. The prompt-only variant improves over TI+LoRA on every dataset, confirming that MLLM-derived descriptions provide a stronger conditioning signal than sparse labels alone. However, CRAFT remains consistently higher than TI+LoRA+ $t_{ep}$ . This supports that reward optimization contributes beyond semantic prompt enrichment.

Table 2: Prompt-only enrichment ablation.

Dataset	TI+LoRA	+ $t_{ep}$	CRAFT
Fitzpatrick17k	.376	.390	<b>.417</b>
CheXpert	.354	.365	<b>.401</b>
BreakHis	.402	.406	<b>.417</b>
ORIGA	.497	.501	<b>.515</b>

Table 3: Additional validation evidence. (a) CRAFT remains strongest under MetaCLIP2 and does not fall into the lowest-diversity regime. (b) CRAFT achieves the highest structured checklist pass rate under an external medical evaluator.

(a) Evaluator robustness and diversity					(b) Checklist audit			
Dataset	Method	SigLIP CAS	MetaCLIP2 CAS	LPIPS	Dataset	Zero-shot	TI+LoRA	CRAFT
CheXpert	TI	0.320	0.356	0.528	Fitzpatrick	0.199	0.580	<b>0.586</b>
	DPO	0.320	0.355	0.529	CheXpert	0.066	0.476	<b>0.566</b>
	TI+LoRA	0.354	0.387	0.466	BreakHis	0.638	0.692	<b>0.811</b>
	<b>CRAFT</b>	<b>0.401</b>	<b>0.417</b>	0.510	ORIGA	0.892	0.912	<b>0.996</b>
Fitzpatrick	TI	0.327	0.368	0.559				
	DPO	0.331	0.371	0.562				
	TI+LoRA	0.376	0.413	0.543				
	<b>CRAFT</b>	<b>0.417</b>	<b>0.456</b>	0.552				

#### 4.2.4 Qualitative analysis

Appendix K provides qualitative comparisons across Fitzpatrick17k, CheXpert, BreakHis, and ORIGA. In Figure 9, CRAFT more often expresses diagnosis-consistent visual patterns than the baselines, including melanoma border irregularity and color variegation, target-like erythema multiforme morphology, pneumonia-like localized opacity, cardiomegaly-related cardiac enlargement, histopathology tissue structure, and optic-disc morphology. These examples are qualitative support rather than definitive clinical evidence. Appendix O further reports representative CheXpert failure cases, including missing fine-grained pathology cues, diagnosis-inconsistent morphology, and clinically incomplete outputs.

#### 4.2.5 Downstream utility in a real and synthetic training setting

We test whether improved alignment translates into practical utility. In a real and synthetic augmentation setting with 20% synthetic samples per batch, following Wang et al. [2025], CRAFT achieves the best downstream accuracy across all four datasets and three data scales (Figure 3). This includes full-data gains over the best baseline on Fitzpatrick17k (0.664 vs. 0.656), CheXpert (0.570 vs. 0.566), BreakHis (0.838 vs. 0.795), and ORIGA (0.801 vs. 0.791). We do not treat classifier improvement as standalone evidence of medical correctness, since synthetic images can aid training while still containing artifacts. Instead, downstream utility provides complementary evidence that the CAS gains are not merely evaluator-specific. Appendix G further shows that method-level CAS is strongly correlated with downstream accuracy and macro-F1 on Fitzpatrick17k and CheXpert.

#### 4.2.6 Physician preference evaluation

To complement automated metrics, we conducted a blinded physician preference study on CheXpert. Two physicians independently ranked synthetic images from different methods across 100 randomly selected cases. As shown in Figure 5, CRAFT is ranked first in 67% of cases, and CAS is strongly associated with Bradley–Terry preference scores derived from physician rankings. We frame this as supporting evidence rather than definitive clinical validation, given the limited scope (one modality, two raters).

#### 4.2.7 Additional validation: evaluator robustness, diversity, and checklist auditing

Three concerns about CAS gains require evidence: evaluator overfitting, reduced sample diversity, and incomplete diagnostic content. We address each in turn. Table 3 provides two complementary checks. First, we evaluate with MetaCLIP2, an out-of-family image–text encoder not used during training, and report prompt-level LPIPS over 4 samples for each of 100 held-out prompts. Method ranking is unchanged under MetaCLIP2 on both datasets, and CRAFT retains the strongest alignment.

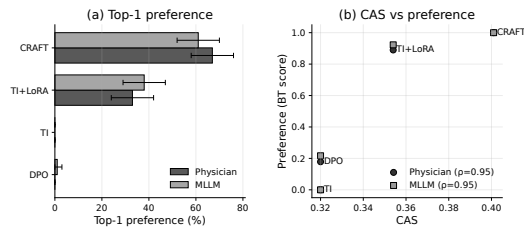


Figure 5: Physician preference evaluation on CheXpert. Two physicians ranked 100 randomized cases. CRAFT has the highest top-1 preference rate (67%), and CAS correlates with Bradley–Terry preference scores.



Table 4: Ablation on Fitzpatrick17k. Left: adding a single reward to the base model. Right: leave-one-out from full CRAFT. Each component primarily affects its intended primitive.

(a) Single-component addition						(b) Leave-one-out					
Variant	VDC	CCS	DD	SFS	CAS	Variant	VDC	CCS	DD	SFS	CAS
Base	.094	.150	.449	.809	.376	<b>Full</b>	<b>.166</b>	<b>.158</b>	<b>.520</b>	<b>.824</b>	<b>.417</b>
+ VDC	<b>.164</b>	.145	.468	.813	.398	w/o DD	.161	.156	.471	.815	.401
+ CCS	.128	<b>.156</b>	.507	.813	.401	w/o Diff.	.163	.153	.492	.819	.407
+ DD	.136	.149	<b>.514</b>	.812	.403	w/o VDC	.151	.156	.517	.817	.410
+ SFS	.130	.148	.470	<b>.820</b>	.392	w/o CCS	.164	.146	.510	.823	.411
						w/o SFS	.164	.158	.520	.820	.416

LPIPS also shows no evidence of severe mode collapse: CRAFT does not fall into the lowest-diversity regime among trained methods. Second, structured checklist auditing with Lingshu [Xu et al., 2025], an external medical evaluator not used in training, shows that CRAFT achieves the highest pass rate across all four datasets, with clear gains on CheXpert (+0.090 over TI+LoRA) and BreakHis (+0.119). We also compare against recent zero-shot general-purpose generators in Appendix L. CRAFT outperforms the strongest zero-shot reference, Flux, on both Fitzpatrick17k (0.417 vs. 0.213 CAS) and CheXpert (0.401 vs. 0.305 CAS). Finally, because CRAFT uses a reference-anchored SFS reward during training, we test for training-set memorization in Appendix M. Across SSIM/pHash duplicate detection and DINOv2 [Oquab et al., 2023] nearest-neighbor analysis, we find no evidence of pixel-level or feature-space memorization.

### 4.3 Ablation study

Each reward component primarily affects its intended primitive (Table 4). In the incremental setting, adding VDC, CCS, DD, and SFS most strongly improves VDC, CCS, DD, and SFS, respectively. In the leave-one-out setting, removing DD causes the largest DD drop (0.520→0.471), removing VDC causes the largest VDC drop (0.166→0.151), and removing CCS causes the largest CCS drop (0.158→0.146). Aggregate CAS shifts are smaller because CAS averages four primitives. The pattern supports the reward decomposition: the components are complementary, not redundant. Appendix J further shows that performance is stable across a broad range of DD reward weights.

**Additional appendix analyses.** Several additional analyses support the main findings. Appendices D–E provide physician and MLLM preference protocols, Appendix F reports few-shot results, Appendices I–J analyze hyperparameter and DD-weight sensitivity, and Appendix N reports label distributions used for metric-based evaluation.

## 5 Limitations

Several limitations remain. First, both reward optimization and evaluation depend on pretrained foundation models; encoder biases or coverage gaps may affect scoring even with our separation between MedSigLIP (training reward) and SigLIP/MetaCLIP2 (evaluation). Second, CAS is a proxy for clinical alignment, not a substitute for expert review. Third, SFS requires paired reference images during training and reference-based evaluation. Our memorization analysis finds no evidence of training-image copying but does not constitute a formal privacy guarantee, which would require differential-privacy or membership-inference analysis. Finally, physician evaluation is limited to CheXpert and two medical doctors.

## 6 Conclusions

We introduced CRAFT, a reward-aligned finetuning framework that adapts diffusion models toward clinically aligned medical image synthesis. CRAFT combines label-driven semantic enrichment with differentiable rewards for visual description consistency, clinical criteria satisfaction, diagnostic discriminability, and semantic feature similarity. Across four medical imaging domains, CRAFT improves average CAS, downstream classification performance, and the low-alignment tail of per-image CAS, indicating fewer hallucination-like or clinically implausible generations under our proxy metric. Together with out-of-family evaluator analysis, diversity measurement, structured checklist

auditing, and physician preference results on CheXpert, these findings indicate that optimizing clinically motivated reward components is a productive path toward reliable medical image generation.

## References

- Josh Achiam, Steven Adler, Sandhini Agarwal, Lama Ahmad, Ilge Akkaya, Florencia Leoni Aleman, Diogo Almeida, Janko Altenschmidt, Sam Altman, Shyamal Anadkat, et al. Gpt-4 technical report. *arXiv preprint arXiv:2303.08774*, 2023.
- Hazrat Ali, Shafaq Murad, and Zubair Shah. Spot the fake lungs: Generating synthetic medical images using neural diffusion models. In *Irish Conference on Artificial Intelligence and Cognitive Science*, pages 32–39. Springer, 2022.
- Pamela G Anderson, Hannah Tarder-Stoll, Mehmet Alpaslan, Nora Keathley, David L Levin, Srivas Venkatesh, Elliot Bartel, Serge Sicular, Scott Howell, Robert V Lindsey, et al. Deep learning improves physician accuracy in the comprehensive detection of abnormalities on chest x-rays. *Scientific reports*, 14(1):25151, 2024.
- Jiamu Bai, Xin Yu, Meilong Xu, Weitao Lu, Xin Pan, Kiwan Maeng, Daniel Kifer, Jian Wang, and Yu Wang. Towards better optimization for listwise preference in diffusion models. *arXiv preprint arXiv:2510.01540*, 2025.
- Mikołaj Bińkowski, Danica J Sutherland, Michael Arbel, and Arthur Gretton. Demystifying mmd gans. *arXiv preprint arXiv:1801.01401*, 2018.
- Kevin Black, Michael Janner, Yilun Du, Ilya Kostrikov, and Sergey Levine. Training diffusion models with reinforcement learning. *arXiv preprint arXiv:2305.13301*, 2023.
- Titus J Brinker, Achim Hekler, Alexander H Enk, Joachim Klode, Axel Hauschild, Carola Berking, Bastian Schilling, Sebastian Haferkamp, Dirk Schadendorf, Stefan Fröhling, et al. A convolutional neural network trained with dermoscopic images performed on par with 145 dermatologists in a clinical melanoma image classification task. *European Journal of Cancer*, 111:148–154, 2019.
- Yung-Sung Chuang, Yang Li, Dong Wang, Ching-Feng Yeh, Kehan Lyu, Ramya Raghavendra, James Glass, Lifei Huang, Jason Weston, Luke Zettlemoyer, et al. Meta clip 2: A worldwide scaling recipe. *arXiv preprint arXiv:2507.22062*, 2025.
- Yunsung Chung, Janet Wang, and Jihun Hamm. Bridging the gap: Synthetic data augmentation through inversion and distribution matching for few-shot learning. In *Proceedings of the 4th International Conference on AI-ML Systems*, pages 1–5, 2024.
- Yunsung Chung, Yunbei Zhang, Nassir Marrouche, and Jihun Hamm. Sok: Can synthetic images replace real data? a survey of utility and privacy of synthetic image generation. *arXiv preprint arXiv:2506.19360*, 2025.
- Kevin Clark, Paul Vicol, Kevin Swersky, and David J Fleet. Directly fine-tuning diffusion models on differentiable rewards. *arXiv preprint arXiv:2309.17400*, 2023.
- Joseph Paul Cohen, Margaux Luck, and Sina Honari. Distribution matching losses can hallucinate features in medical image translation. In *International conference on medical image computing and computer-assisted intervention*, pages 529–536. Springer, 2018.
- Bram De Wilde, Anindo Saha, Maarten de Rooij, Henkjan Huisman, and Geert Litjens. Medical diffusion on a budget: textual inversion for medical image generation. *arXiv preprint arXiv:2303.13430*, 2023.
- Andre Esteva, Brett Kuprel, Roberto A Novoa, Justin Ko, Susan M Swetter, Helen M Blau, and Sebastian Thrun. Dermatologist-level classification of skin cancer with deep neural networks. *nature*, 542(7639):115–118, 2017.
- Jamil Fayyad, Nourhan Bayasi, Ziyang Yu, and Homayoun Najjaran. Lesiongen: A concept-guided diffusion model for dermatology image synthesis. In *MICCAI Workshop on Deep Generative Models*, pages 3–12. Springer, 2025.

- Rinon Gal, Yuval Alaluf, Yuval Atzmon, Or Patashnik, Amit H Bermano, Gal Chechik, and Daniel Cohen-Or. An image is worth one word: Personalizing text-to-image generation using textual inversion. *arXiv preprint arXiv:2208.01618*, 2022.
- Matthew Groh, Caleb Harris, Luis Soenksen, Felix Lau, Rachel Han, Aerin Kim, Arash Koochek, and Omar Badri. Evaluating deep neural networks trained on clinical images in dermatology with the fitzpatrick 17k dataset. In *Proceedings of the IEEE/CVF conference on computer vision and pattern recognition*, pages 1820–1828, 2021.
- Pengfei Guo, Can Zhao, Dong Yang, Ziyue Xu, Vishwesh Nath, Yucheng Tang, Benjamin Simon, Mason Belue, Stephanie Harmon, Baris Turkbey, et al. Maisi: Medical ai for synthetic imaging. In *2025 IEEE/CVF Winter Conference on Applications of Computer Vision (WACV)*, pages 4430–4441. IEEE, 2025.
- Jack Hessel, Ari Holtzman, Maxwell Forbes, Ronan Le Bras, and Yejin Choi. Clipscore: A reference-free evaluation metric for image captioning. In *Proceedings of the 2021 conference on empirical methods in natural language processing*, pages 7514–7528, 2021.
- Martin Heusel, Hubert Ramsauer, Thomas Unterthiner, Bernhard Nessler, and Sepp Hochreiter. Gans trained by a two time-scale update rule converge to a local nash equilibrium. *Advances in neural information processing systems*, 30, 2017.
- Jonathan Ho, Ajay Jain, and Pieter Abbeel. Denoising diffusion probabilistic models. *Advances in neural information processing systems*, 33:6840–6851, 2020.
- Edward J Hu, Yelong Shen, Phillip Wallis, Zeyuan Allen-Zhu, Yuanzhi Li, Shean Wang, Lu Wang, Weizhu Chen, et al. Lora: Low-rank adaptation of large language models. *ICLR*, 1(2):3, 2022.
- Peng Huang, Xue Gao, Lihong Huang, Jing Jiao, Xiaokang Li, Yuanyuan Wang, and Yi Guo. Chest-diffusion: a light-weight text-to-image model for report-to-cxr generation. In *2024 IEEE International Symposium on Biomedical Imaging (ISBI)*, pages 1–5. IEEE, 2024.
- Jeremy Irvin, Pranav Rajpurkar, Michael Ko, Yifan Yu, Silvana Ciurea-Ilcus, Chris Chute, Henrik Marklund, Behzad Haghgoo, Robyn Ball, Katie Shpanskaya, et al. Chexpert: A large chest radiograph dataset with uncertainty labels and expert comparison. In *Proceedings of the AAAI conference on artificial intelligence*, volume 33, pages 590–597, 2019.
- Firas Khader, Gustav Müller-Franzes, Soroosh Tayebi Arasteh, Tianyu Han, Christoph Haarbuerger, Maximilian Schulze-Hagen, Philipp Schad, Sandy Engelhardt, Bettina Baeßler, Sebastian Foersch, et al. Denoising diffusion probabilistic models for 3d medical image generation. *Scientific Reports*, 13(1):7303, 2023.
- Gwanghyun Kim, Taesung Kwon, and Jong Chul Ye. Diffusionclip: Text-guided diffusion models for robust image manipulation. In *Proceedings of the IEEE/CVF conference on computer vision and pattern recognition*, pages 2426–2435, 2022.
- Diederik P Kingma and Max Welling. Auto-encoding variational bayes. *arXiv preprint arXiv:1312.6114*, 2013.
- Ira Ktena, Olivia Wiles, Isabela Albuquerque, Sylvestre-Alvise Rebuffi, Ryutaro Tanno, Abhijit Guha Roy, Shekoofeh Azizi, Danielle Belgrave, Pushmeet Kohli, Taylan Cemgil, et al. Generative models improve fairness of medical classifiers under distribution shifts. *Nature Medicine*, 30(4): 1166–1173, 2024.
- Binxu Li, Minkai Xu, Jiaqi Han, Meihua Dang, and Stefano Ermon. Divergence minimization preference optimization for diffusion model alignment. *arXiv preprint arXiv:2507.07510*, 2025.
- Dongxu Li, Junnan Li, and Steven Hoi. Blip-diffusion: Pre-trained subject representation for controllable text-to-image generation and editing. *Advances in Neural Information Processing Systems*, 36:30146–30166, 2023.
- Shufan Li, Konstantinos Kallidromitis, Akash Gokul, Yusuke Kato, and Kazuki Kozuka. Aligning diffusion models by optimizing human utility. *Advances in Neural Information Processing Systems*, 37:24897–24925, 2024.

- Yuan Liu, Ayush Jain, Clara Eng, David H Way, Kang Lee, Peggy Bui, Kimberly Kanada, Guilherme de Oliveira Marinho, Jessica Gallegos, Sara Gabriele, et al. A deep learning system for differential diagnosis of skin diseases. *Nature medicine*, 26(6):900–908, 2020.
- Maxime Oquab, Timothée Darcet, Théo Moutakanni, Huy Vo, Marc Szafraniec, Vasil Khalidov, Pierre Fernandez, Daniel Haziza, Francisco Massa, Alaaeldin El-Nouby, et al. Dinov2: Learning robust visual features without supervision. *arXiv preprint arXiv:2304.07193*, 2023.
- Walter HL Pinaya, Petru-Daniel Tudosiu, Jessica Dafflon, Pedro F Da Costa, Virginia Fernandez, Parashkev Nachev, Sebastien Ourselin, and M Jorge Cardoso. Brain imaging generation with latent diffusion models. In *MICCAI workshop on deep generative models*, pages 117–126. Springer, 2022.
- Rafael Rafailov, Archit Sharma, Eric Mitchell, Christopher D Manning, Stefano Ermon, and Chelsea Finn. Direct preference optimization: Your language model is secretly a reward model. *Advances in neural information processing systems*, 36:53728–53741, 2023.
- Robin Rombach, Andreas Blattmann, Dominik Lorenz, Patrick Esser, and Björn Ommer. High-resolution image synthesis with latent diffusion models. In *Proceedings of the IEEE/CVF conference on computer vision and pattern recognition*, pages 10684–10695, 2022.
- Nataniel Ruiz, Yuanzhen Li, Varun Jampani, Yael Pritch, Michael Rubinstein, and Kfir Aberman. Dreambooth: Fine tuning text-to-image diffusion models for subject-driven generation. In *Proceedings of the IEEE/CVF conference on computer vision and pattern recognition*, pages 22500–22510, 2023.
- Tim Salimans, Ian Goodfellow, Wojciech Zaremba, Vicki Cheung, Alec Radford, and Xi Chen. Improved techniques for training gans. *Advances in neural information processing systems*, 29, 2016.
- Parham Saremi, Amar Kumar, Mohamed Mohamed, Zahra TehraniNasab, and Tal Arbel. R14med-ddpo: reinforcement learning for controlled guidance towards diverse medical image generation using vision-language foundation models. In *International Conference on Medical Image Computing and Computer-Assisted Intervention*, pages 478–488. Springer, 2025.
- Andrew Sellergren, Sahar Kazemzadeh, Tiam Jaroensri, Atilla Kiraly, Madeleine Traverse, Timo Kohlberger, Shawn Xu, Fayaz Jamil, Cían Hughes, Charles Lau, et al. Medgemma technical report. *arXiv preprint arXiv:2507.05201*, 2025.
- Luis R Soenksen, Timothy Kassis, Susan T Conover, Berta Marti-Fuster, Judith S Birkenfeld, Jason Tucker-Schwartz, Asif Naseem, Robert R Stavert, Caroline C Kim, Maryanne M Senna, et al. Using deep learning for dermatologist-level detection of suspicious pigmented skin lesions from wide-field images. *Science Translational Medicine*, 13(581):eabb3652, 2021.
- Shenghuan Sun, Greg Goldgof, Atul Butte, and Ahmed M Alaa. Aligning synthetic medical images with clinical knowledge using human feedback. *Advances in Neural Information Processing Systems*, 36:13408–13428, 2023.
- Bram Wallace, Meihua Dang, Rafael Rafailov, Linqi Zhou, Aaron Lou, Senthil Purushwalkam, Stefano Ermon, Caiming Xiong, Shafiq Joty, and Nikhil Naik. Diffusion model alignment using direct preference optimization. In *Proceedings of the IEEE/CVF Conference on Computer Vision and Pattern Recognition*, pages 8228–8238, 2024.
- Janet Wang, Yunsung Chung, Zhengming Ding, and Jihun Hamm. From majority to minority: A diffusion-based augmentation for underrepresented groups in skin lesion analysis. In *International Conference on Medical Image Computing and Computer-Assisted Intervention*, pages 14–23. Springer, 2024.
- Janet Wang, Yunbei Zhang, Zhengming Ding, and Jihun Hamm. Doctor approved: Generating medically accurate skin disease images through ai-expert feedback. *arXiv preprint arXiv:2506.12323*, 2025.
- Juanying Xie, Ran Liu, Joseph Luttrell IV, and Chaoyang Zhang. Deep learning based analysis of histopathological images of breast cancer. *Frontiers in genetics*, 10:80, 2019.

- Jiazheng Xu, Xiao Liu, Yuchen Wu, Yuxuan Tong, Qinkai Li, Ming Ding, Jie Tang, and Yuxiao Dong. Imagereward: Learning and evaluating human preferences for text-to-image generation. *Advances in Neural Information Processing Systems*, 36:15903–15935, 2023.
- Weiwen Xu, Hou Pong Chan, Long Li, Mahani Aljunied, Ruifeng Yuan, Jianyu Wang, Chenghao Xiao, Guizhen Chen, Chaoqun Liu, Zhaodonghui Li, et al. Lingshu: A generalist foundation model for unified multimodal medical understanding and reasoning. *arXiv preprint arXiv:2506.07044*, 2025.
- Yanwu Xu, Li Sun, Wei Peng, Shuyue Jia, Katelyn Morrison, Adam Perer, Afroz Zandifar, Shyam Visweswaran, Motahhare Eslami, and Kayhan Batmanghelich. Medsyn: text-guided anatomy-aware synthesis of high-fidelity 3-d ct images. *IEEE Transactions on Medical Imaging*, 43(10): 3648–3660, 2024.
- Hu Ye, Jun Zhang, Sibao Liu, Xiao Han, and Wei Yang. Ip-adapter: Text compatible image prompt adapter for text-to-image diffusion models. *arXiv preprint arXiv:2308.06721*, 2023.
- Xiaohua Zhai, Basil Mustafa, Alexander Kolesnikov, and Lucas Beyer. Sigmoid loss for language image pre-training. In *Proceedings of the IEEE/CVF international conference on computer vision*, pages 11975–11986, 2023.
- Lvmin Zhang, Anyi Rao, and Maneesh Agrawala. Adding conditional control to text-to-image diffusion models. In *Proceedings of the IEEE/CVF international conference on computer vision*, pages 3836–3847, 2023.
- Richard Zhang, Phillip Isola, Alexei A Efros, Eli Shechtman, and Oliver Wang. The unreasonable effectiveness of deep features as a perceptual metric. In *Proceedings of the IEEE conference on computer vision and pattern recognition*, pages 586–595, 2018.
- Zhuo Zhang, Feng Shou Yin, Jiang Liu, Wing Kee Wong, Ngan Meng Tan, Beng Hai Lee, Jun Cheng, and Tien Yin Wong. Origa-light: An online retinal fundus image database for glaucoma analysis and research. In *2010 Annual international conference of the IEEE engineering in medicine and biology*, pages 3065–3068. IEEE, 2010.
- Can Zhao, Pengfei Guo, Dong Yang, Yucheng Tang, Yufan He, Benjamin Simon, Mason Belue, Stephanie Harmon, Baris Turkbey, and Daguang Xu. Maisi-v2: Accelerated 3d high-resolution medical image synthesis with rectified flow and region-specific contrastive loss. *arXiv preprint arXiv:2508.05772*, 2025.

# Appendix

---

## Table of Contents

- **A. Implementation details and reproducibility**
    - A.1 Clinical alignment module (CAM)
    - A.2 Diagnostic discriminability linear probe
    - A.3 Statistical uncertainty
    - A.4 Compute resources
    - A.5 Code and data access
  - **B. Prompt enrichment pipeline**
    - B.1 Label conditioning to prevent diagnosis hallucination
    - B.2 Schema enforcement across domains
  - **C. Clinical checklists**
    - C.1 Fitzpatrick17k clinical checklists
    - C.2 CheXpert clinical checklists
    - C.3 BreakHis clinical checklists
    - C.4 ORIGA clinical checklists
  - **D. Physician preference evaluation**
  - **E. Automated preference-based evaluation**
  - **F. Few-shot adaptation**
  - **G. CAS–downstream utility correlation**
  - **H. Low-alignment tail analysis**
  - **I. Hyperparameter sensitivity analysis**
  - **J. Diagnostic discriminability weight sensitivity**
  - **K. Extended qualitative results**
  - **L. Comparison with general-purpose zero-shot generators**
  - **M. Memorization analysis**
  - **N. Dataset label distributions**
  - **O. Error analysis on CheXpert**
  - **P. Existing assets and licenses**
  - **Q. Broader impact**
- 

## A Implementation details and reproducibility

### A.1 Clinical alignment module (CAM)

The CAM uses a frozen medical VLM as a differentiable critic. We employ MedSigLIP-448 (<https://huggingface.co/google/medsiglip-448>) as the backbone VLM. All image and text embeddings used in Eq. (2–5) are extracted from this model. The VLM is kept fully frozen throughout CRAFT training and is used only to compute reward signals. No gradients are backpropagated into the VLM parameters. Given a generated image and its associated textual inputs, CAM outputs four scalar rewards corresponding to visual description consistency, clinical criteria satisfaction, diagnostic discriminability, and semantic feature similarity.

Table 5: CAS uncertainty over five seeds. Values are mean  $\pm$  standard deviation. ORIGA standard deviations are reported when seed-level logs are available.

Method	Fitzpatrick17k	CheXpert	BreakHis	ORIGA
Zero-Shot	.202 $\pm$ .004	.205 $\pm$ .006	.294 $\pm$ .003	.363 $\pm$ .007
DPO	.331 $\pm$ .004	.320 $\pm$ .004	.378 $\pm$ .005	.462 $\pm$ .005
TI	.327 $\pm$ .003	.320 $\pm$ .004	.367 $\pm$ .003	.456 $\pm$ .004
TI+LoRA	.376 $\pm$ .003	.354 $\pm$ .005	.402 $\pm$ .002	.497 $\pm$ .005
CRAFT	.417 $\pm$ .002	.401 $\pm$ .003	.417 $\pm$ .003	.515 $\pm$ .004

Table 6: Approximate compute used for the main experiment families. GPU-hours are approximate and are reported to indicate scale rather than exact accounting.

Experiment family	Scope	Hardware	Approximate runtime	Seeds	Approx. GPU-hours
Textual inversion	Disease-token learning for class-conditioned generation	1 GPU per class	$\sim$ 0.9 h per class on CheXpert	1	$\sim$ 3.6
TI+LoRA finetuning	Standard adaptation baseline and prompt-enriched variant	1 GPU per run	$\sim$ 10–11 min per CheXpert run	1	$\sim$ 0.4
CRAFT finetuning	Reward-aligned finetuning and component / hyperparameter sweeps	1 GPU per run	$\sim$ 1.3 h per CheXpert run; $\sim$ 8–9 h per Fitzpatrick17k run	train seed 42; evaluation over 5 seeds	$\sim$ 50–55
CAS / evaluator scoring	SigLIP CAS scoring, diagnostic-probe evaluation, and MetaCLIP2 reevaluation	1 GPU	$\sim$ 1 min per CheXpert seed; $\sim$ 5 min per Fitzpatrick17k seed	5	$<$ 1 for main tables
Downstream augmentation	Real-synthetic classifier training across datasets and data scales	1 GPU per run	$\sim$ 1–2 min per classifier run	1–3 depending on setting	$\sim$ 1–2
Checklist auditing	External medical-evaluator checklist pass-rate analysis	1 GPU per run	$\sim$ 2.5–3 h per audit run	N/A	$\sim$ 8–9
Preference evaluation	MLLM-based candidate ranking and physician-preference aggregation	1 GPU for MLLM judging	$\sim$ 7–15 min for MLLM judging batches	N/A	$<$ 1 for MLLM judging

## A.2 Diagnostic discriminability linear probe

The diagnostic integrity reward  $r_{dd}$  (Eq. 4) is implemented using a linear probe trained on frozen VLM embeddings. A single linear layer is trained using only the real training split of each dataset. We use Adam optimizer with learning rate  $1 \times 10^{-3}$  for 50 epochs and batch size of 256. During CRAFT optimization, the linear layer is kept frozen and used only to compute reward gradients with respect to the diffusion model. During training, the probe provides log-likelihood rewards for stable gradient optimization, while we report classification accuracy as a diagnostic discriminability metric during evaluation. We train two diagnostic linear probes with the same protocol but on different embedding spaces: a MedSigLIP-space probe for the differentiable DD reward during CRAFT training, and a SigLIP-space probe for metric computation. Both probes are trained only on real training images and kept frozen during generation or evaluation.

## A.3 Statistical uncertainty

For synthetic-method CAS, we report mean and standard deviation over five random seeds. The main table reports means for compactness, and Table 5 provides the corresponding CAS uncertainty where available. For physician preference evaluation, we report 95% bootstrap confidence intervals. These uncertainty estimates quantify run-to-run variability and evaluator-sampling variability, not clinical uncertainty.

## A.4 Compute resources

All experiments were run on NVIDIA RTX 6000 Ada GPUs. Table 6 summarizes the approximate compute used for the main experiment families. Runtimes vary by dataset size, number of generated samples, and evaluator choice; when exact wall-clock logs were unavailable, we estimated runtimes from checkpoint or output-file timestamps.

## A.5 Code and data access

We release anonymized code at <https://anonymous.4open.science/r/CRAFT-07B4>. The repository includes training scripts, evaluation scripts, configuration files, and table/figure generation code. Raw medical images are not redistributed. Users should obtain Fitzpatrick17k, CheXpert, BreakHis, and ORIGA from their original sources and comply with the corresponding licenses or data-use agreements. We provide dataset preprocessing instructions, split definitions where redistribution is permitted, and scripts for regenerating enriched prompts, checklists, synthetic images, and CAS metrics.

## B Prompt enrichment pipeline

To ensure the generated enriched prompts ( $t_{ep}$ ) and checklists ( $t_c$ ) are consistent and high-quality, we implement a strict generation pipeline using GPT-4o [Achiam et al., 2023]. The process is governed by two key mechanisms: Label Conditioning and Schema Enforcement.

### B.0.1 Label conditioning to prevent hallucination

A common failure mode in medical VLM captioning is ungrounded diagnosis inference, where the model hallucinates a condition based on visual effects. To mitigate this, we provide the ground-truth label  $y$  as a hard constraint in the system prompt. The model is instructed to describe the visual sign of the provided label  $y$  within the image  $x$ , rather than attempting to predict  $y$ . This encourages the generated descriptions to remain consistent with the provided label and reduces unsupported diagnostic inference, although the resulting descriptions remain automatically generated and may still contain imperfect visual details.

### B.0.2 Schema enforcement

We enforce strict output schemas to standardize the vocabulary across the dataset and filter out malformed responses.

- **Dermatology (Fitzpatrick17k):** We constrain the *body part* and *skin type* fields to a closed set of values (e.g., fair, brown, dark) to prevent uncontrolled vocabulary expansion and long-tail descriptor fragmentation.
- **Histopathology (BreakHis):** We constrain tissue context and key findings to a fixed schema tailored to breast histopathology morphology at  $100\times$  magnification. This reduces unsupported free-form pathology language and keeps descriptions focused on patch-visible architectural and cytologic features.
- **Radiology (CheXpert):** We use label-dependent logic to prevent pathology leakage. For example, if the ground truth is "No Finding", the system prompt explicitly forbids the generation of terms like "opacity" or "consolidation", ensuring the caption remains "clear lungs with sharp costophrenic angles."
- **Ophthalmology (ORIGA):** We constrain optic-disc findings to a fixed glaucoma-oriented schema, including cup size, neuroretinal rim status, vessel course, and peripapillary changes. This prevents free-form ophthalmology language and keeps descriptions focused on visible fundus features relevant to glaucomatous optic neuropathy.



### System Prompt Logic for Dermatology (Fitzpatrick17k)

You're an expert dermatologist. You extract visual morphology from ONE clinical image. The ground truth diagnosis is provided below as {label}. Do not invent findings outside of this diagnosis.

Return STRICTLY valid JSON with keys:

- body\_part (MUST be one of: {allowed\_body\_parts})
- lesion\_features (concise phrase  $\leq$  20 words: shape, texture, color)

Style constraints:

- Use plain language. Avoid medical jargon (say "red" not "erythematous").
- Focus on visual attributes of {label} (shape, border, color).
- Output JSON only. No markdown.

### System Prompt Logic for Histopathology (BreakHis)

You're an expert breast pathologist. You describe ONE H&E breast histopathology patch at 100x magnification.

The ground-truth diagnosis is provided below as {label}. Do not predict a diagnosis. Do not invent findings outside of this diagnosis. Only mention morphology that is reasonably visible in a single 100x patch.

Return STRICTLY valid JSON with keys:

- tissue\_context
- key\_findings
- visual\_summary

Schema rules:

- tissue\_context: MUST be one of ["glandular", "fibroepithelial", "stromal", "papillary", "mucinous", "infiltrative", "mixed"]
- key\_findings: comma-separated list chosen ONLY from {allowed\_key\_findings}
- visual\_summary: concise phrase  $\leq$  18 words

Style constraints:

- Use visual morphology only.
- Prefer short pathology terms such as "enlarged acini", "slit-like ducts", "leaf-like stromal fronds", "tightly packed tubules", "irregular ducts", "single-file cells", "mucin pools", "papillary fronds", and "fibrovascular cores".
- Do not mention biomarkers, grade, mitotic rate, receptor status, prognosis, or treatment.
- Do not mention features that cannot be supported by the patch.
- Avoid long sentences and differential diagnosis language.
- Output JSON only. No markdown.

### System Prompt Logic for Radiology (CheXpert)

You're an expert radiologist. Describe a frontal chest x-ray using simple visual language. The ground truth diagnosis is provided below as {label}. Do not invent findings outside of this diagnosis.

Return STRICTLY valid JSON with keys:

- devices (e.g., "pacemaker", "picc line", or "none")
- key\_findings (comma-separated list from allowed pool)
- visual\_summary (concise phrase  $\leq 16$  words)

Style constraints:

- Avoid Negations: Do NOT say "no pleural effusion". Instead, say "sharp costophrenic angles".
- Prefer positive descriptors (e.g., "clear lungs") for normal regions.
- If label="No Finding", forbid pathology terms entirely.
- Output JSON only. No markdown.

### System Prompt Logic for Ophthalmology (ORIGA)

You're an expert ophthalmologist. You describe ONE retinal fundus image.

The ground-truth diagnosis is provided below as {label}. Do not predict a diagnosis. Do not invent findings outside of this diagnosis. Only mention morphology that is reasonably visible in a single fundus photograph.

Return STRICTLY valid JSON with keys:

- disc\_appearance
- key\_findings
- visual\_summary

Schema rules:

- disc\_appearance: MUST be one of ["normal disc", "enlarged cup", "rim thinning", "notched rim", "glaucomatous disc"]
- key\_findings: comma-separated list chosen ONLY from {allowed\_key\_findings}
- visual\_summary: concise phrase  $\leq 18$  words

Style constraints:

- Use only visible fundus morphology.
- Focus on optic cup size, neuroretinal rim, vessel course, and peripapillary changes.
- Do not mention visual field loss, intraocular pressure, OCT, prognosis, or treatment.
- Do not mention features not clearly supported by the image.
- Output JSON only. No markdown.

## C Clinical checklists

### C.1 Fitzpatrick17k clinical checklists

Table 7 details the structured visual criteria used to guide the Clinical Alignment Module (CAM). We decompose complex dermatological pathology into five fundamental visual attributes (Location, Lesion Type, Shape/Size, Color, Texture) to ensure interpretability by the general-domain VLMs. These attributes were selected to balance clinical completeness with interpretability by general-domain vision-language models.

Table 7: Structured Clinical Criteria for Fitzpatrick 17k Classes.

<b>Condition</b>	<b>Attribute</b>	<b>Visual Description</b>
<b>Acne</b>	Location	Face, forehead, chest, shoulders, upper back
	Lesion Type	Bumps including comedones (whiteheads, blackheads) and inflamed pimples
	Shape/Size	Small clogged-pore bumps; larger tender nodules/cysts
	Color	Red or skin-colored bumps; blackheads have dark plug
	Texture	Oily or shiny skin; pus or crust if ruptured
<b>Actinic Keratosis</b>	Location	Sun-exposed areas (face, scalp, ears, hands)
	Lesion Type	Rough, scaly patch or small crusty bump
	Shape/Size	Flat or slightly raised, under 2.5 cm
	Color	Pink, red, or brownish; yellowish crust
	Texture	Dry, coarse, sandpaper-like surface
<b>Allergic Contact Dermatitis</b>	Location	Contact sites (hands, face, neck)
	Lesion Type	Red patches with blisters or swelling
	Shape/Size	Irregular shape following exposure
	Color	Pink to red; purple/brown on dark skin
	Texture	Weepy, crusty, or scaly
<b>Basal Cell Carcinoma</b>	Location	Sun-exposed areas (face, nose, ears, neck, scalp, shoulders)
	Lesion Type	Pearly or waxy bump/nodule, or flat scaly patch with a raised edge
	Shape/Size	Small, round/oval; can ulcerate or develop a central depression
	Color	Translucent or pearly on fair skin; brown/black or glossy dark on darker skin
	Texture	Smooth, shiny surface; can crust or scab with central ulceration
<b>Eczema</b>	Location	Flexural areas (inner elbows, behind knees), hands, neck, eyelids
	Lesion Type	Patches or plaques, sometimes with small blisters or bumps
	Shape/Size	Ill-defined patches varying in size; often bilateral or symmetric
	Color	Red or pink on lighter skin; purple, gray, or dark brown on darker skin
	Texture	Dry, flaky, or scaly; can become thick and leathery (lichenification)
<b>Erythema Multiforme</b>	Location	Hands, feet, arms, legs; mucous membranes (lips, mouth)
	Lesion Type	Target (bull's-eye) lesions with concentric rings
	Shape/Size	Round lesions (1–3 cm) with dark center, pale ring, and outer red ring
	Color	Dark red/purple center, pale ring, red outer zone; gray/dark on dark skin
<b>Folliculitis</b>	Location	Hair-bearing areas (beard, scalp, underarms, legs, buttocks)
	Lesion Type	Small pustules or red papules centered around hair follicles

Continued on next page

	Shape/Size	Clusters of 2–5 mm bumps; each usually pierced by a hair
	Color	Red/pink (light skin); dark/hyperpigmented (dark skin); white/yellow pus
	Texture	Dome-shaped, often fluid-filled top; crusts if ruptured
<b>Granuloma Annulare</b>	Location	Hands, feet, wrists, ankles; occasionally trunk-/limbs
	Lesion Type	Smooth, firm bumps (papules) forming rings
	Shape/Size	Annular (ring-shaped) up to few cm; composed of small papules
	Color	Skin-colored, pink, or reddish; purple/brown on darker skin
	Texture	Generally smooth surface; little to no flaking or scale
<b>Keloid</b>	Location	Chest, shoulders, earlobes, jawline, or sites of injury
	Lesion Type	Overgrown scar tissue extending beyond original wound
	Shape/Size	Raised, irregular shape; can grow large and claw-like
	Color	Pink/red (light skin); dark brown, purple, or black (dark skin)
	Texture	Smooth, hairless, firm, rubbery, or shiny surface
<b>Lichen Planus</b>	Location	Wrists, forearms, ankles, lower back, mucous membranes
	Lesion Type	Flat-topped papules; can form plaques
	Shape/Size	Polygonal, 2–10 mm papules
	Color	Violaceous (purple); gray-brown or hyperpigmented on dark skin
	Texture	Shiny surface with fine white lines (Wickham's striae)
<b>Lupus Erythematosus</b>	Location	Face (butterfly rash), scalp, ears, sun-exposed areas
	Lesion Type	Malar rash (flat/raised); discoid lesions (scaly/scarred)
	Shape/Size	Butterfly shape across nose/cheeks; discoid are coin-shaped
	Color	Pink-red; can be dark red or hyperpigmented on darker skin
	Texture	Smooth (malar) or rough/scaly with central scarring (discoid)
<b>Melanoma</b>	Location	Trunk, limbs, face, nails; in darker skin, often on palms/soles
	Lesion Type	Atypical mole or patch; irregular shape and color
	Shape/Size	Asymmetric, often >6 mm, with irregular or notched borders
	Color	Multiple shades (brown, black, red, white, blue); variegated
	Texture	Smooth early; may become raised, crusted, or ulcerated if advanced
<b>Mycosis Fungoides</b>	Location	Non-sun-exposed areas (buttocks, thighs); can be widespread
	Lesion Type	Patches (eczema-like), plaques (thick), or tumor nodules

Continued on next page

		Shape/Size Color	Irregular patches/plaques; tumors can be large Pink-red to reddish-brown; dark/hyperpigmented on dark skin
		Texture	Dry, scaly, wrinkled (cigarette paper) patches; tumors smooth/ulcerated
<b>Pityriasis Rosea</b>	Location		Trunk (back, chest, abdomen); "Christmas tree" pattern
	Lesion Type		Single "Herald patch" followed by smaller oval lesions
	Shape/Size		Herald patch (2–6 cm); daughter lesions (1–2 cm ovals)
	Color		Pink/salmon (light skin); gray, brown, or violet (dark skin)
	Texture		Fine "collarette" scale at the inner edge of lesions
<b>Prurigo Nodularis</b>	Location		Arms, legs, upper back (areas reachable for scratching)
	Lesion Type		Firm, extremely itchy nodules
	Shape/Size		Dome-shaped nodules 1–3 cm; often multiple
	Color		Pink, red, or skin-toned; often dark brown/black borders
	Texture		Hard, warty, or crusted surface; often excoriated (scratched)
<b>Psoriasis</b>	Location		Elbows, knees, scalp, lower back; can affect nails, palms, soles
	Lesion Type		Well-demarcated plaques with thick, scaly surface
	Shape/Size		Round/oval or irregular plaques; range from small patches to large areas
	Color		Pink/red with silvery scales (light skin); purple/brown with gray scales (dark skin)
	Texture		Dry, flaky scales that can be peeled off; underlying skin may bleed
<b>Sarcoidosis</b>	Location		Face, shins, scars
	Lesion Type		Firm plaques or nodules
	Shape/Size		Broad plaques; 1-5 cm nodules
	Color		Red-brown; purple; discoloration
	Texture		Smooth, firm, rubbery
<b>Scabies</b>	Location		Finger webs, wrists, waist
	Lesion Type		Linear burrows and small allergic papules/vesicles
	Shape/Size		Burrows (5–15 mm wavy lines); small bumps (1–2 mm)
	Color		Skin-toned, pink, or red; dark spots on darker skin
	Texture		Burrows feel like slight ridges; crusting from scratching
<b>Squamous Carcinoma</b>	<b>Cell</b>	Location	Sun-exposed areas (face, ears, lips, hands), scars
		Lesion Type	Crusty bump, ulcer, or thick plaque
		Shape/Size	Firm nodule or patch; often >1 cm; can be crater-like
		Color	Pink/red base; brown/dark on dark skin; white keratin
		Texture	Rough, scaly, hyperkeratotic; may bleed or ulcerate
<b>Vitiligo</b>	Location		Face (eyes, mouth), hands, feet, arms, legs, genitals
	Lesion Type		Depigmented patches with well-defined borders

Continued on next page

Shape/Size	Irregular shapes; can start small and enlarge; often symmetrical
Color	Completely white or pale; high contrast against surrounding skin
Texture	Normal skin texture (no scaling or thickening), only color is lost

## C.2 CheXpert clinical checklists

For the radiological domain, we adapt the Color attribute to represent radiographic opacity and density. As shown in Table 8, we translate specific pathologies (e.g., Pleural Effusion) into geometric primitives (e.g., Meniscus sign, Homogeneous opacity) to maximize alignment with the VLM’s visual priors.

Table 8: Structured Clinical Criteria for CheXpert Classes.

Condition	Attribute	Visual Description
<b>No Finding</b>	Location	Entire chest field (Lungs, Heart, Pleura)
	Lesion Type	Normal anatomy; no pathological opacities
	Shape/Size	Heart size normal (<50% chest width); sharp triangular costophrenic angles
	Color	Lungs are dark (radiolucent); bones/heart are bright white
	Texture	Clear lung fields with fine vascular markings; no haziness
<b>Cardiomegaly</b>	Location	Central chest (Mediastinum/Heart)
	Lesion Type	Enlargement of the cardiac silhouette
	Shape/Size	Globular or widened heart shadow; width >50% of rib cage
	Color	Enlarged central white opacity
	Texture	Smooth, distinct heart borders; vascular congestion may be present
<b>Pneumonia</b>	Location	Focal area in lungs (often asymmetric, lobar, or segmental)
	Lesion Type	Consolidation or Infiltrate (filled airspaces)
	Shape/Size	Patchy, irregular cloud-like shape; fluffy or ill-defined borders
	Color	Increased whiteness (opacity) against dark lung background
	Texture	Fluffy or hazy “ground glass” appearance; may show air bronchograms
<b>Pleural Effusion</b>	Location	Lung bases (bottom corners) or lining the chest wall
	Lesion Type	Fluid accumulation masking the diaphragm
	Shape/Size	Meniscus sign (U-shaped curve); blunting of sharp costophrenic angle
	Color	Dense, homogeneous white opacity
	Texture	Smooth, uniform density (water-like); obscures the lung base

## C.3 BreakHis clinical checklists

For histopathology, we define structured visual criteria that describe tissue context, lesion type, architectural pattern, color, and texture. As shown in Table 9, these criteria are designed to capture class-defining morphology at 100× magnification while remaining interpretable to a vision–language critic. Compared with dermatology and radiology, the emphasis here is less on gross anatomy and more on glandular structure, stromal organization, and characteristic epithelial arrangements.

Table 9: Structured Histopathology Criteria for BreakHis Classes.

<b>Condition</b>	<b>Attribute</b>	<b>Visual Description</b>
<b>Adenosis</b>	Tissue Context	Lobulocentric glandular units with crowded acini in fibrous stroma
	Lesion Type	Benign proliferative glandular lesion with enlarged acini
	Shape/Size	Numerous small round acini with relatively regular lumina; clustered lobular pattern
	Color	Pink eosinophilic stroma with blue-purple uniform epithelial nuclei
	Texture	Orderly gland architecture; smooth outlines; bland cytology
<b>Fibroadenoma</b>	Tissue Context	Fibroepithelial lesion with ducts embedded in fibrous stroma
	Lesion Type	Well-circumscribed biphasic benign lesion
	Shape/Size	Round to slit-like ducts compressed by stroma; pushing contours
	Color	Pale pink collagenous stroma with evenly basophilic epithelial nuclei
	Texture	Smooth fibrous background; bland epithelium; low atypia
<b>Phyllodes Tumor</b>	Tissue Context	Fibroepithelial lesion with epithelial-lined stromal clefts
	Lesion Type	Leaf-like stromal fronds projecting into clefted spaces
	Shape/Size	Elongated branching fronds and cleft-like spaces; broader architecture than fibroadenoma
	Color	Pink stromal fronds with blue-purple epithelial and stromal nuclei
	Texture	Undulating leaf-like contours; more cellular stroma; mixed epithelial-stromal pattern
<b>Tubular Adenoma</b>	Tissue Context	Gland-forming lesion dominated by tightly packed tubules
	Lesion Type	Benign tubular epithelial proliferation
	Shape/Size	Numerous small round or oval tubules with open lumina; minimal intervening stroma
	Color	Pink scant stroma with blue-purple uniform nuclei around luminal spaces
	Texture	Dense orderly tubular pattern; smooth gland borders; bland cytology
<b>Ductal Carcinoma</b>	Tissue Context	Infiltrative epithelial lesion within fibrotic or desmoplastic stroma
	Lesion Type	Malignant duct-forming carcinoma
	Shape/Size	Irregular angulated ducts, nests, or cords with variable lumina
	Color	Hyperchromatic blue-purple nuclei in pink desmoplastic stroma
	Texture	Crowded pleomorphic cells; jagged infiltrative architecture; reduced uniformity
<b>Lobular Carcinoma</b>	Tissue Context	Discohesive infiltrating cells in fibrous stroma, often around ducts or lobules
	Lesion Type	Malignant lobular-type infiltrate

Continued on next page

		Shape/Size	Single-file cords and targetoid periductal arrangement; little tubule formation
		Color	Small dark nuclei scattered through pale to pink stroma
		Texture	Loose discohesive pattern; subtle infiltrative spread; monotonous small cells
<b>Mucinous Carcinoma</b>		Tissue Context	Tumor cell clusters suspended within extracellular mucin pools
		Lesion Type	Mucin-producing carcinoma
		Shape/Size	Rounded clusters or strips of cells floating in large mucin lakes
		Color	Pale blue to lightly basophilic mucin with darker tumor cell nuclei
		Texture	Smooth gelatinous background; low-density floating cellular islands; soft lobulated spaces
<b>Papillary Carcinoma</b>		Tissue Context	Papillary epithelial proliferation organized around fibrovascular cores
		Lesion Type	Malignant papillary lesion
		Shape/Size	Branching papillary fronds with central fibrovascular stalks
		Color	Pink fibrovascular cores lined by blue-purple crowded epithelial cells
		Texture	FronD-like branching surface; layered epithelium; delicate core structures

Table 10: ORIGA Clinical Checklists.

<b>Condition</b>	<b>Attribute</b>	<b>Visual Description</b>
<b>Normal</b>	Optic Disc	Small to moderate optic cup with balanced cup-to-disc ratio and preserved neuroretinal rim
	Rim	Neuroretinal rim appears circumferentially intact without focal thinning or notching
	Vessels	Retinal vessels near the disc follow a normal course without marked nasalization or bayoneting
	Peripapillary Region	No obvious nerve fiber layer defect, disc hemorrhage, or glaucomatous peripapillary change
	Overall Fundus	Overall retinal fundus appearance is consistent with a non-glaucomatous eye
<b>Glaucoma</b>	Optic Disc	Enlarged optic cup or increased vertical cup-to-disc ratio is visible
	Rim	Neuroretinal rim shows focal or diffuse thinning, notching, or clear rim loss, especially in the superior or inferior rim
	Vessels	Retinal vessels near the disc show nasalization, bayoneting, or displacement around the cup edge
	Peripapillary Region	Peripapillary nerve fiber layer loss, disc hemorrhage, or localized glaucomatous change is visible or suspiciously present
	Overall Fundus	Overall optic nerve head appearance is consistent with glaucomatous optic neuropathy



Table 11: Separation of model roles to mitigate evaluation leakage.

Component	Prompt/Checklist Gen.	Reward/Optimization	Metric Computation	Purpose
MLLM (text)	✓	×	×	enriched prompts, checklists
MLLM (ranking)	×	×	✓	preference rankings
MedSigLIP (CAM)	×	✓	×	differentiable clinical reward
SigLIP (metrics)	×	×	✓	VDC/CCS/SFS/DD/CAS metrics

## D Physician preference evaluation

For radiology (CheXpert), we conduct a blinded preference study using two medical doctors. Each physician evaluates 100 randomly selected cases. For each case, images generated by all methods are presented in randomized order without method identifiers. Physicians produce a strict ranking from best to worst based on clinical plausibility and visual realism. We aggregate rankings with a Bradley–Terry model to compute method-level preference scores and confidence intervals. Main results are shown in Figure 5.

Physicians were shown the following instruction: “For each case, you will see the target diagnosis and anonymized synthetic images generated by different methods in randomized order. Please rank the images from best to worst according to clinical plausibility, diagnostic consistency with the target label, anatomical realism, and overall image quality. Do not attempt to identify the generation method.” No method names were shown during evaluation. The interface consisted of a randomized image grid with rank-entry fields; screenshots are omitted because the interface contained no additional task information. The physicians were not additionally compensated for this evaluation.

## E Automated preference-based evaluation

In addition to metric-based evaluation, we provide an automated preference analysis using an MLLM as an independent judge. The MLLM is used only for evaluation and is not involved in training or reward computation. This analysis is intended as supporting evidence and does not replace the physician evaluation reported for CheXpert.

For each test case, the MLLM is presented with (i) the target diagnosis, (ii) the textual prompt used for synthesis, and (iii) four synthetic candidate images generated by different methods. Candidates are presented in randomized order and labeled A to D. The MLLM is instructed to produce a strict ranking of the four candidates from best to worst based on clinical plausibility, visual realism, and consistency with the provided description.

The ranking criteria are adapted to each domain. For radiology data (CheXpert), the MLLM is instructed to act as an expert radiologist and evaluate candidates according to diagnostic accuracy (whether the image correctly exhibits the target pathology) and visual realism (anatomical structure, texture, and noise characteristics consistent with real chest X-rays). For dermatology data (Fitzpatrick17k), the MLLM is instructed to act as an expert dermatologist and evaluate candidates based on clinical accuracy (characteristic lesion morphology, border irregularity, and color variation) and visual realism (skin texture, hair, and lighting consistency).

We report two complementary views of automated preference. First, we compute the top-1 selection rate, defined as the fraction of cases in which a method is ranked first by the MLLM. Second, we aggregate full rankings across cases using a BT model to obtain a continuous preference score for each method. We do not use any textual outputs from the MLLM for scoring or supervision. All quantitative analysis is based exclusively on the predicted rankings. Figure 6 and Figure 7 summarize the resulting automated preference analysis on Fitzpatrick17k.

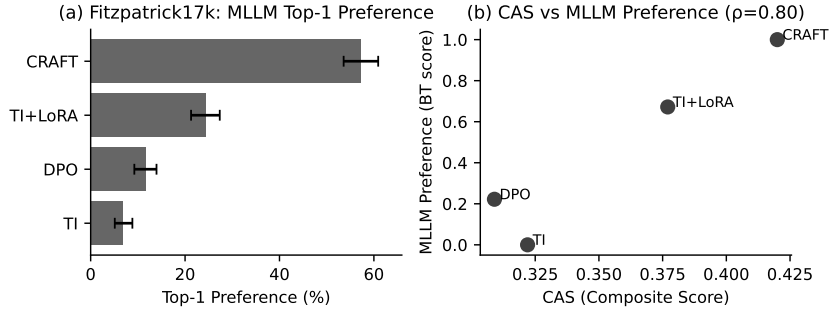


Figure 6: Automated MLLM-based preference analysis on Fitzpatrick17k. (a) Top-1 preference rate with 95% confidence intervals. (b) Correlation between the Clinical Alignment Score (CAS) and MLLM-derived Bradley–Terry preference scores across methods.

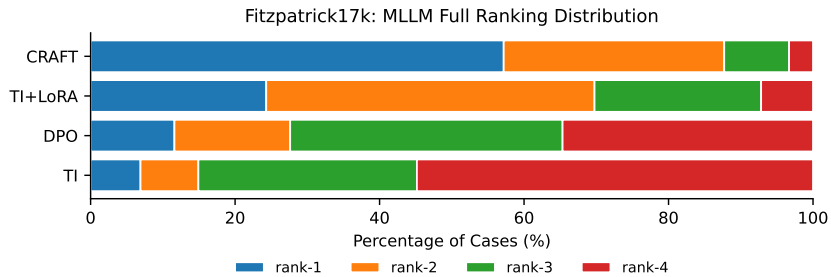


Figure 7: Automated ranking distribution on Fitzpatrick17k using an MLLM judge. Each bar shows the percentage of cases in which a method is ranked at each position (Rank 1 to Rank 4).

## F Few-shot adaptation

To test whether CRAFT remains effective in more data-limited settings, we evaluate 10-shot and 20-shot adaptation on Fitzpatrick17k, CheXpert, BreakHis, and ORIGA. Table 12 shows that CRAFT remains the best-performing method across all four datasets and both shot regimes.

## G CAS–downstream utility correlation

To test whether CAS tracks practical downstream utility, we compute the correlation between method-level CAS and downstream classifier performance across five shared methods.

## H Low-alignment tail analysis

In addition to the main-text CDF in Figure 4, we report full per-method tail statistics. For each dataset, the low-CAS threshold  $\tau$  is defined as the 25th percentile of the real-image CAS distribution. This avoids imposing a single absolute threshold across modalities with different visual complexity and evaluator score scales.

Table 14 reports the full per-method low-CAS rates and 10th-percentile CAS values. CRAFT reduces the low-alignment region across all four datasets.

Table 12: Few-shot CAS under low-data adaptation across four datasets. CRAFT remains the best-performing method in both 10-shot and 20-shot regimes.

Dataset	Shots	TI	DPO	TI+LoRA	CRAFT
Fitzpatrick17k	10-shot	0.287	0.229	0.316	<b>0.338</b>
Fitzpatrick17k	20-shot	0.301	0.242	0.342	<b>0.350</b>
CheXpert	10-shot	0.220	0.293	0.278	<b>0.353</b>
CheXpert	20-shot	0.237	0.298	0.340	<b>0.363</b>
BreakHis	10-shot	0.363	0.364	0.371	<b>0.378</b>
BreakHis	20-shot	0.364	0.368	0.373	<b>0.381</b>
ORIGA	10-shot	0.319	0.341	0.346	<b>0.374</b>
ORIGA	20-shot	0.376	0.413	0.415	<b>0.453</b>

Table 13: Correlation between CAS and downstream classifier metrics.

Dataset	Metric	Pearson $r$	$p$	Spearman $\rho$	$p$
Fitzpatrick17k	Accuracy	0.974	0.005	0.900	0.037
	Macro-F1	0.951	0.013	0.900	0.037
CheXpert	Accuracy	0.972	0.006	0.667	0.219
	Macro-F1	0.968	0.007	0.821	0.089

## I Hyperparameter sensitivity analysis

We investigate the sensitivity of CRAFT to three key hyperparameters on the CheXpert dataset: the number of gradient steps ( $K$ ), training sampling steps ( $T_{train}$ ), and gradient estimation repeats ( $M$ ). Figure 8 summarizes these results.

**Gradient Steps ( $K$ ).** We observe that a single gradient step ( $K = 1$ ) shows the highest performance (CAS: 0.3977) with a degradation as  $K$  increases (0.3815 at  $K = 4$ ). This reflects the difficulty of backpropagating through the diffusion process for multiple update steps which introduces optimization instability due to compounding variance in the gradient estimation.

**Sampling Steps ( $T_{train}$ ).** Increasing sampling fidelity improves performance initially, peaking at  $T = 20$  (CAS: 0.4011). Interestingly, further increasing  $T$  to 50 yields no benefit (0.3934). This shows that a coarse SDE approximation (DDPM) is sufficient to capture the correct gradient direction.

**Repeats ( $M$ ).** Using  $M = 2$  repeats slightly improves performance over a single pass by reducing gradient variance (0.3978 vs. 0.3977). Further increasing  $M$  provides a negligible benefit while linearly increasing training cost. Minimizing this variance too aggressively may cause the model to overfit, thereby reducing its ability to generalize.

## J Diagnostic discriminability weight sensitivity

Because the diagnostic discriminability term differs in scale and form from the cosine-similarity rewards, we additionally sweep its weight on CheXpert. As shown in Table 15, performance remains stable across a broad range of  $\lambda_{DD}$  values, with the default setting  $\lambda_{DD} = 0.20$  achieving the best DD and CAS. This shows that CRAFT is not overly fragile to reasonable reward-weight choices.

## K Extended qualitative results

We provide additional qualitative comparisons to complement the main paper and illustrate representative synthesis behavior across methods. These examples highlight clinically relevant visual attributes such as lesion morphology, border definition, color variation, and consistency of texture in dermatology, as well as anatomical structure and pathologically appropriate opacity patterns in radiology (see Figure 9).

Figures 11, 12, 13, and 14 present additional samples on Fitzpatrick17k, CheXpert, BreakHis, and ORIGA, respectively. Alongside visual realism, the comparisons emphasize whether generated

Table 14: Low-alignment tail analysis. We report two complementary views of the lower tail of the per-image CAS distribution: the fraction of generated samples with CAS below  $\tau$ , where  $\tau$  is the 25th percentile of the Real reference CAS distribution for each dataset, and the 10th percentile of each method’s per-image CAS distribution. CRAFT consistently reduces the low-alignment tail across all four datasets, indicating fewer hallucination-like or clinically implausible generations under our proxy metric.

Dataset	$\tau$ (Real P25)	Method	$n$	Mean CAS $\uparrow$	CAS $< \tau$ $\downarrow$	10th pct. CAS $\uparrow$
Fitzpatrick17k	0.310	Zero-Shot	3100	0.202	90.0%	0.109
		DPO	3100	0.331	64.4%	0.205
		TI	3100	0.327	64.7%	0.203
		TI+LoRA	3100	0.376	54.2%	0.230
		CRAFT	3100	<b>0.417</b>	<b>48.7%</b>	<b>0.234</b>
CheXpert	0.314	Zero-Shot	495	0.205	73.5%	0.122
		DPO	495	0.320	75.6%	0.235
		TI	495	0.320	74.5%	0.232
		TI+LoRA	495	0.354	68.9%	0.279
		CRAFT	495	<b>0.401</b>	<b>60.8%</b>	<b>0.281</b>
BreakHis	0.530	Zero-Shot	1041	0.294	99.0%	0.183
		DPO	1041	0.378	86.8%	0.252
		TI	1041	0.367	98.3%	0.183
		TI+LoRA	1041	0.402	89.0%	0.244
		CRAFT	1041	<b>0.417</b>	<b>52.1%</b>	<b>0.283</b>
ORIGA	0.564	Zero-Shot	196	0.363	100.0%	0.187
		DPO	196	0.462	100.0%	0.291
		TI	196	0.456	94.9%	0.243
		TI+LoRA	196	0.497	89.8%	0.294
		CRAFT	196	<b>0.515</b>	<b>77.0%</b>	<b>0.306</b>

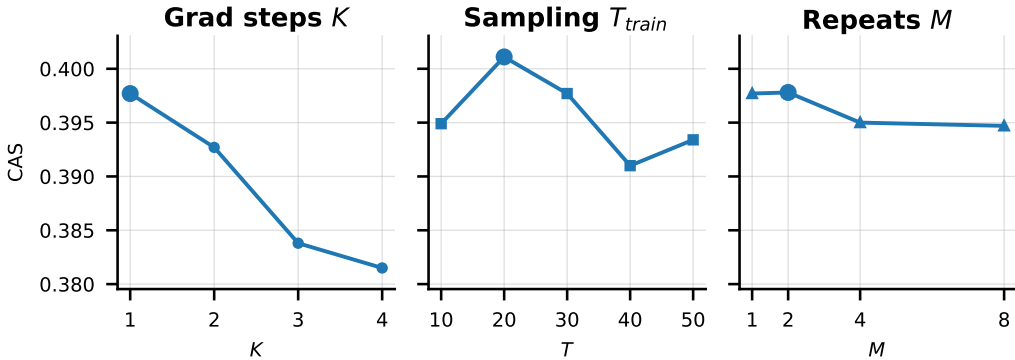


Figure 8: Hyperparameter sensitivity analysis on CheXpert. Left: number of gradient backpropagation steps ( $K$ ); Middle: number of diffusion sampling steps during training ( $T_{train}$ ); Right: number of gradient estimation repeats ( $M$ ). We select  $K = 1$ ,  $T_{train} = 20$ , and  $M = 2$  as a balanced configuration.

images express diagnosis-consistent features and avoid ambiguous or conflicting findings that can arise when optimizing primarily for visual plausibility.

## L Comparison with general-purpose zero-shot generators

Our main experiments compare adaptation methods on a shared Stable Diffusion v2.1 backbone to isolate the effect of clinical reward-aligned finetuning. As an additional reference, we compare against recent general-purpose zero-shot generators in Table 16. Flux is the strongest zero-shot reference, but CRAFT achieves substantially higher CAS on both Fitzpatrick17k and CheXpert. This

Table 15: Sensitivity to the Diagnostic Discriminability (DD) reward weight on CheXpert.

$\lambda_{DD}$	DD	CAS
0.02	0.342	0.393
0.10	0.361	0.398
0.20	<b>0.375</b>	<b>0.401</b>
0.50	0.365	0.398
1.00	0.357	0.395

Table 16: CAS comparison against recent zero-shot general-purpose generators.

Method	Fitzpatrick17k CAS	CheXpert CAS
Janus-Pro	0.159	0.203
Flux	0.213	0.305
SD 2.1 Zero-Shot	0.202	0.205
<b>CRAFT</b>	<b>0.417</b>	<b>0.401</b>

shows that larger general-purpose generators do not automatically yield stronger alignment with clinically motivated criteria in our medical prompt-conditioned setting.

## M Memorization analysis

Because SFS encourages alignment between generated samples and real reference images in MedSigLIP embedding space during training, a natural concern is whether this induces memorization of training images. We evaluate this concern through two complementary tests using held-out test-prompt generations.

**Pixel-space near-duplicate detection.** We compute structural similarity (SSIM) and perceptual hash (pHash) distance between each generated sample and every training image, and count near-duplicates using  $SSIM > 0.95$  or pHash Hamming distance  $\leq 5$ . Table 17 reports the results. No method on any dataset produces any sample with  $SSIM > 0.95$  to a training image. On CheXpert, CRAFT and TI+LoRA each show 2 pHash-near-duplicates out of 200 generations, indicating no CRAFT-specific memorization signal. CRAFT’s maximum SSIM is at or below baseline methods on BreakHis and ORIGA, including the smallest dataset ORIGA with 454 training images. These results show no evidence that CRAFT produces verbatim or near-verbatim copies of training images.

**Feature-space nearest-neighbor distance in an independent encoder.** We embed all generated, training, and held-out test images using DINOv2-base, a self-supervised vision encoder that is independent from the SigLIP family used for CAS computation and from the MedSigLIP critic used during CRAFT training. For each generated sample, we compute the cosine distance to its nearest training neighbor ( $d_{NN}^{train}$ ) and nearest test neighbor ( $d_{NN}^{test}$ ). Memorization would manifest as  $d_{NN}^{train} \ll d_{NN}^{test}$ , since memorized generations would collapse onto specific training images while remaining farther from unseen test images. Table 18 shows that across all four datasets, both CRAFT and TI+LoRA produce nearly symmetric distances to train and test sets, with  $|\Delta| < 0.012$  for every method-dataset pair. On ORIGA, the smallest dataset, CRAFT’s train-test gap ( $-0.0037$ ) is smaller in magnitude than TI+LoRA’s ( $-0.0111$ ), indicating that CRAFT does not exhibit greater training-set proximity than the standard adaptation baseline.

On BreakHis and ORIGA, CRAFT generations are substantially closer to real images than TI+LoRA in DINOv2 space. Critically, this proximity is symmetric across train and test splits, indicating that CRAFT learns distributional structure of real medical images rather than memorizing specific training samples. Combined with the absence of SSIM near-duplicates in Table 17, these results suggest that SFS improves distributional alignment without inducing training-set copying.

## N Dataset label distributions

We report label distributions for the real training and test splits together with the synthetic datasets used for metric-based evaluation, to make class composition explicit and support reproducibility. For

Table 17: Pixel-space near-duplicate detection. We compute SSIM and pHash Hamming distance between each generated sample and every training image. “Any” counts samples flagged by either criterion. No method produces any sample with SSIM > 0.95 to a training image on any dataset.

Dataset	Method	SSIM > 0.95	pHash ≤ 5	Any	Max SSIM
Fitzpatrick17k	TI	0	0	0	0.901
	DPO	0	0	0	0.902
	TI+LoRA	0	0	0	0.909
	CRAFT	0	0	0	0.910
CheXpert	TI	0	0	0	0.843
	DPO	0	0	0	0.834
	TI+LoRA	0	2	2	0.872
	CRAFT	0	2	2	0.883
BreakHis	TI	0	0	0	0.469
	DPO	0	0	0	0.678
	TI+LoRA	0	0	0	0.490
	CRAFT	0	0	0	<b>0.418</b>
ORIGA	TI	0	0	0	0.934
	DPO	0	0	0	0.886
	TI+LoRA	0	0	0	0.929
	CRAFT	0	0	0	<b>0.874</b>

Table 18: Memorization analysis via nearest-neighbor distance in DINOv2 feature space, an independent self-supervised encoder not used during CRAFT training or CAS computation.  $d_{NN}^{train}$  and  $d_{NN}^{test}$  are mean cosine distances from each generated sample to the nearest training and test image, respectively. Memorization would manifest as  $d_{NN}^{train} \ll d_{NN}^{test}$ . All methods show nearly symmetric distances to train and test ( $|\Delta| < 0.012$ ), indicating no train-specific memorization.

Dataset	Method	$d_{NN}^{train}$	$d_{NN}^{test}$	$\Delta = d_{NN}^{train} - d_{NN}^{test}$
Fitzpatrick17k	TI+LoRA	0.1267	0.1350	-0.0083
	CRAFT	0.1303	0.1370	-0.0067
CheXpert	TI+LoRA	0.0255	0.0255	0.0000
	CRAFT	0.0254	0.0259	-0.0005
BreakHis	TI+LoRA	0.1768	0.1757	0.0011
	CRAFT	0.0437	0.0439	-0.0002
ORIGA	TI+LoRA	0.1761	0.1872	-0.0111
	CRAFT	0.1382	0.1419	-0.0037

CAS-based evaluation, synthetic images are generated to match the label distribution of the held-out test split. This enables instance-level comparison without introducing class imbalance as a confound.

Tables 19, 20, 21, and 22 summarize the resulting distributions for Fitzpatrick17k, CheXpert, BreakHis, and ORIGA. This reporting clarifies that observed performance differences arise from image quality and clinical validity rather than unreported differences in class composition.

## O Error analysis on CheXpert

Although CRAFT improves overall clinical alignment, some generated chest X-rays remain clinically unreliable. Figure 10 shows three representative failure modes on CheXpert.

**(1) Missing fine-grained pathology cues despite broadly plausible appearance.** In Case A, the generated image is broadly compatible with cardiomegaly because the cardiomedial silhouette appears somewhat prominent. However, the radiographic detail is insufficient to support the diagnosis confidently. Adjacent left basilar/lateral opacity and partly indistinct cardiac borders limit accurate delineation of the true cardiac contour. As a result, the image appears plausible at a coarse level but lacks the fine-grained cues required for reliable diagnosis.

Table 19: Label distribution for Fitzpatrick17k. Synthetic data are generated to match the held-out test split for metric-based evaluation.

Condition	Train	Test	Synthetic
Psoriasis	326	327	327
Squamous Cell Carcinoma	288	291	291
Lichen Planus	246	245	245
Basal Cell Carcinoma	234	234	234
Allergic Contact Dermatitis	214	215	215
Lupus Erythematosus	205	205	205
Sarcoidosis	173	175	175
Folliculitis	171	171	171
Scabies	169	169	169
Melanoma	130	131	131
Erythema Multiforme	118	118	118
Granuloma Annulare	106	105	105
Eczema	101	102	102
Pityriasis Rosea	96	97	97
Acne	92	91	91
Mycosis Fungoides	91	91	91
Actinic Keratosis	88	87	87
Prurigo Nodularis	85	85	85
Vitiligo	80	83	83
Keloid	78	78	78
<b>Total</b>	<b>3100</b>	<b>3100</b>	<b>3100</b>

Table 20: Label distribution for the CheXpert subset. Synthetic data are generated to match the held-out test split for metric-based evaluation.

Condition	Train	Test	Synthetic
No Finding	125	124	124
Pleural Effusion	125	123	123
Cardiomegaly	123	123	123
Pneumonia	122	125	125
<b>Total</b>	<b>495</b>	<b>495</b>	<b>495</b>

(2) **Morphology inconsistent with the requested diagnosis.** In Case B, the generated image does not exhibit the typical radiographic pattern of pneumonia. There is no clear focal air-space consolidation, no convincing lobar or segmental dense opacity, and no visible air bronchograms, which are common findings supporting pneumonia on chest radiographs. Instead, the lungs remain relatively well aerated, and there is no strong silhouette sign or associated pleural effusion suggesting a focal infectious process.

(3) **Visually plausible but clinically incomplete outputs.** In Case C, the generated image is visually plausible for pleural effusion because the lower lungs show basilar hazy opacity that can superficially resemble pleural fluid. However, the output is clinically incomplete for a confident effusion diagnosis: there is no definite meniscus sign, and the costophrenic angles are not clearly assessable. The finding may also be confused with other causes of basilar opacity or cardiac enlargement. This example illustrates that visual plausibility alone does not guarantee diagnostic completeness.

## P Existing assets and licenses

Table 23 summarizes the existing datasets, models, and code assets used in this work. We cite the original sources and follow the corresponding licenses, terms of use, and data-use agreements. We do not redistribute restricted medical images or model artifacts.

Table 21: Label distribution for the BreakHis subset. Synthetic data are generated to match the held-out test split for metric-based evaluation.

<b>Condition</b>	<b>Train</b>	<b>Test</b>	<b>Synthetic</b>
Adenosis	56	57	57
Ductal Carcinoma	452	451	451
Fibroadenoma	130	130	130
Lobular Carcinoma	85	85	85
Mucinous Carcinoma	111	111	111
Papillary Carcinoma	71	71	71
Phyllodes Tumor	60	61	61
Tubular Adenoma	75	75	75
<b>Total</b>	<b>1040</b>	<b>1041</b>	<b>1041</b>

Table 22: Label distribution for ORIGA.

<b>Condition</b>	<b>Train</b>	<b>Test</b>	<b>Synthetic</b>
Non-Glaucoma	318	132	132
Glaucoma	136	64	64
<b>Total</b>	<b>454</b>	<b>196</b>	<b>196</b>

## Q Broader impact

CRAFT may improve medical image synthesis by encouraging generated images to satisfy clinically motivated criteria rather than visual realism alone. This could support data augmentation and model development in settings where labeled medical images are scarce.

However, synthetic medical images also carry risks. They may contain subtle artifacts, reflect biases from the training datasets or foundation-model evaluators, or be overinterpreted as clinically valid evidence. Misuse could include presenting synthetic images as real clinical data or relying on automated clinical-alignment scores without expert review. We therefore frame CAS as a proxy rather than a clinical ground truth, avoid deployment claims, report failure cases, and include physician preference evaluation only as supporting evidence.



Table 23: Existing assets used in this work. Dataset and model redistribution follows the original license or data-use agreement.

Asset	Role in paper	Source / citation	License or access terms
Fitzpatrick17k	Dermatology dataset	Groh et al. [2021]	Original dataset terms; not redistributed
CheXpert	Chest X-ray dataset	Irvin et al. [2019]	Use original Stanford access terms; not redistributed
BreakHis	Histopathology dataset	Xie et al. [2019]	Use original dataset license / terms
ORIGA	Retinal fundus dataset	Zhang et al. [2010]	Use original dataset license / terms
Stable Diffusion v2.1	Base generator	Stability AI model card	Use original model license / terms
MedSigLIP	Training critic	Sellergren et al. [2025]	Use original model license / terms
SigLIP	Main evaluator	Zhai et al. [2023]	Use original model license / terms
MetaCLIP2	Out-of-family evaluator	Chuang et al. [2025]	Use original model license / terms
TI / LoRA / DPO baselines	Baseline methods	Cited original papers	Use original code/model licenses where applicable

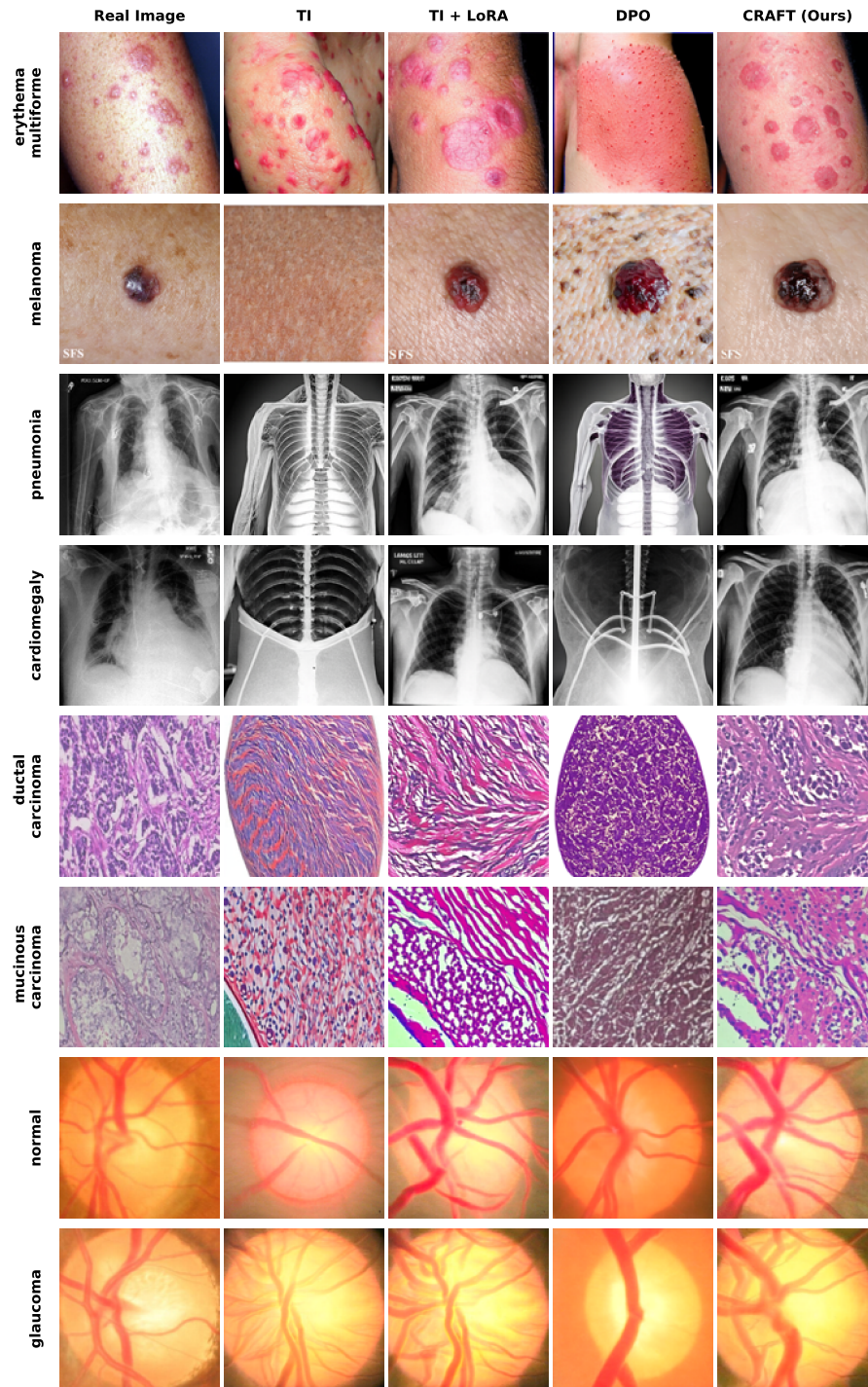


Figure 9: Qualitative comparison across four medical imaging domains: Fitzpatrick17k dermatology, CheXpert chest X-ray, BreakHis histopathology, and ORIGA retinal fundus imaging. Each row shows a real reference image alongside synthetic samples generated by TI [De Wilde et al., 2023], TI+LoRA [Wang et al., 2024], DPO [Wang et al., 2025], and CRAFT. CRAFT more often preserves diagnosis-consistent visual patterns while reducing ambiguous or artifact-heavy generations.

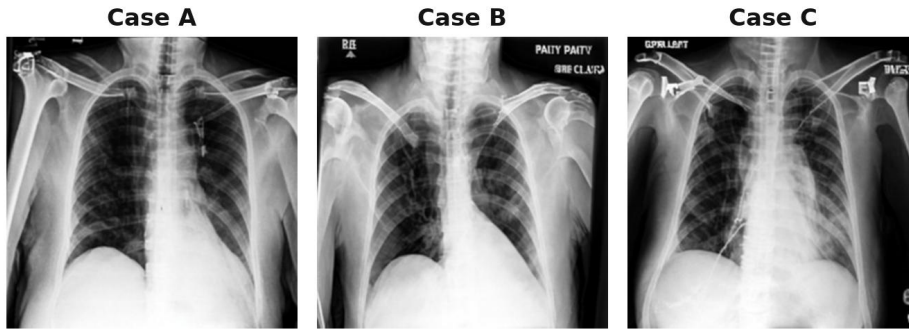


Figure 10: Error analysis on CheXpert. Representative CRAFT failure cases illustrating three residual failure modes: (a) broadly plausible cardiomegaly with insufficient fine-grained contour evidence, (b) requested pneumonia without characteristic focal consolidation, and (c) visually plausible basilar opacity suggestive of pleural effusion but lacking definitive diagnostic signs.



Figure 11: Extended qualitative results on Fitzpatrick17k. Additional randomly selected samples comparing CRAFT against baseline methods.

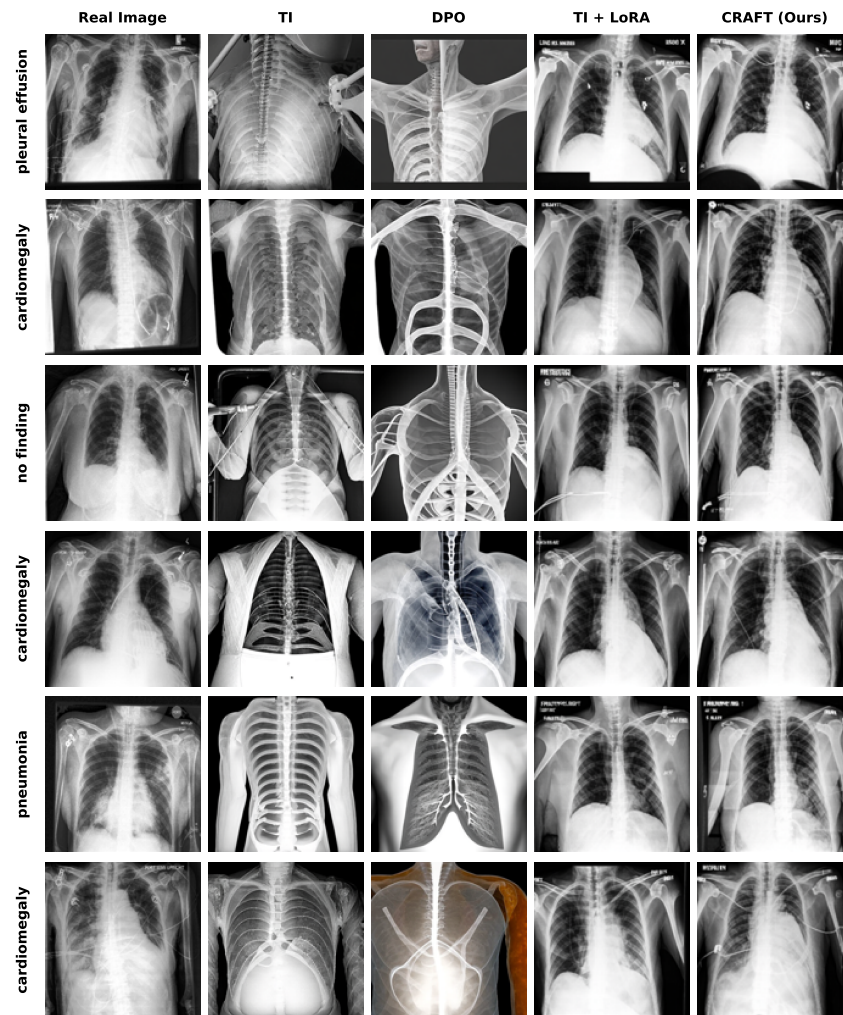


Figure 12: Qualitative results on CheXpert. Randomly selected samples comparing CRAFT against baseline methods.

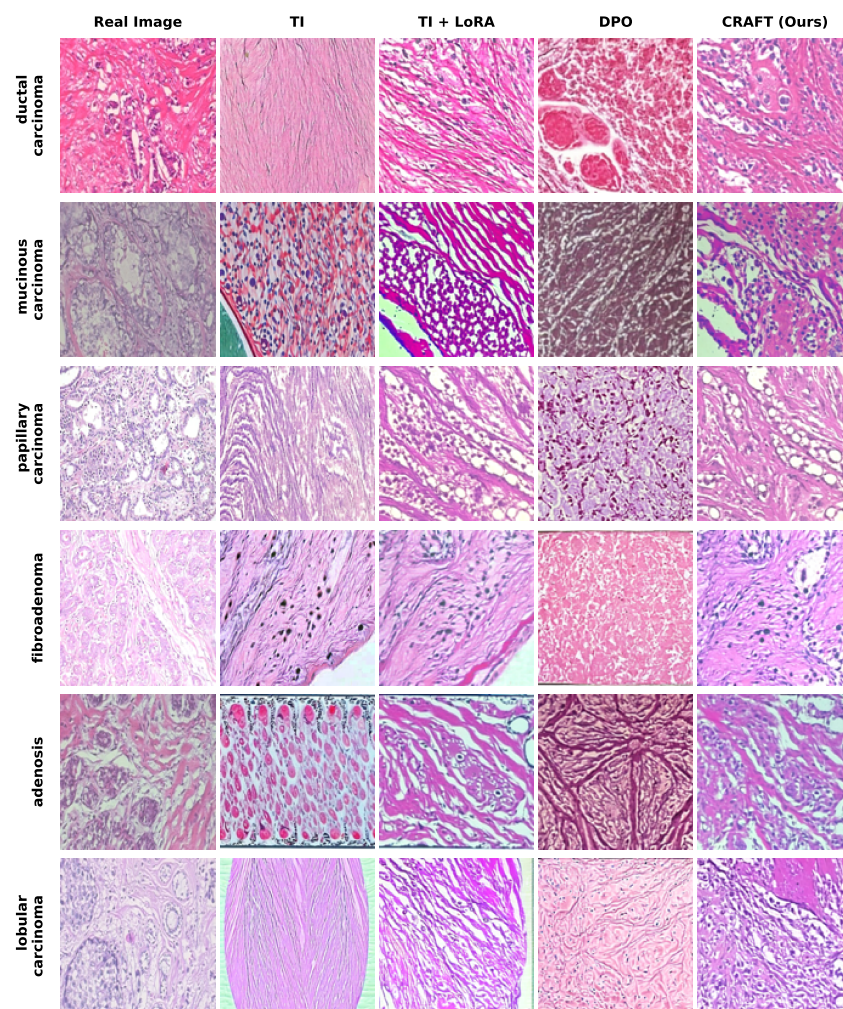


Figure 13: Qualitative results on BreakHis. Randomly selected samples comparing CRAFT against baseline methods.

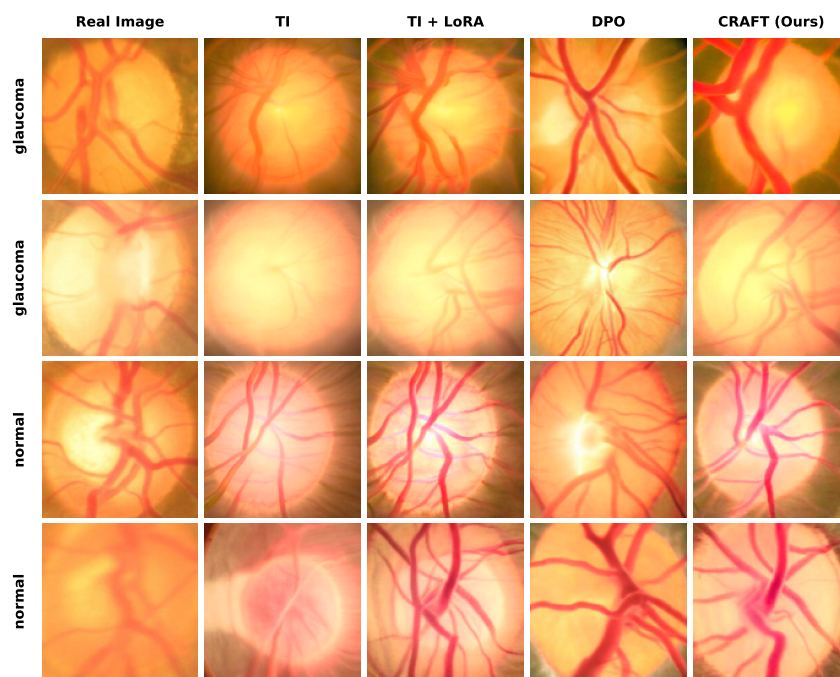


Figure 14: Qualitative results on ORIGA. Randomly selected samples comparing CRAFT against baseline methods.